Seismic performance of self-centering steel frames with SMA-viscoelastic hybrid braces

Cheng Fang[a,c]*, Yiwei Ping[a], Yiyi Chen[a], Michael C H Yam[b,c], Junbai Chen[a], Wei Wang[a]

[a] *State Key Laboratory of Disaster Reduction in Civil Engineering & Department of Structural Engineering, Tongji University, Shanghai 200092, China*

[b] *Department of Building & Real Estate, The Hong Kong Polytechnic University, Hung Hom, Kowloon, Hong Kong, China*

[c] *Chinese National Engineering Research Centre for Steel Construction (Hong Kong Branch), The Hong Kong Polytechnic University, Hong Kong, China*

* Corresponding author: email: chengfang@tongji.edu.cn, Tel: +86 (0)21-65982926

Seismic performance of self-centering steel frames with SMA-viscoelastic hybrid braces

Abstract: This study presents a novel hybrid self-centering system aiming to overcome critical shortcomings identified in the existing self-centering solution. Two types of hybrid brace incorporating shape memory alloy elements and integrated viscoelastic dampers are first introduced, followed by a system-level analysis on a series of prototype buildings. The results show that using viscoelastic material to reach a moderate damping ratio is highly effective in peak and residual deformation control. Floor acceleration is also effectively controlled by the hybrid solution. A parametric study is then conducted, and design recommendations are given. A probability-based residual deformation prediction model is finally proposed.

Keywords: Self-centering; shape memory alloy (SMA); viscoelastic; seismic resilience; steel braced frame; hybrid control.

1. Introduction

In the conventional seismic design, energy dissipation capacity relies significantly on the inelastic behavior of structural members at intended regions. It has been revealed from past major earthquakes that this design philosophy cannot guarantee efficient post-event recoverability. The yielding behavior potentially leads to large residual deformation which is very difficult to deal with, both technically and financially, after an earthquake. For example, more than 90 reinforced concrete (RC) bridge piers with residual drifts exceeding 1% were demolished after the 1995 Kobe earthquake, although they did not collapse [1]. The 2011 Christchurch earthquake led to the demolition of hundreds of buildings which stood still after the earthquake but exhibited unacceptable damages and residual deformation [2]. McCormick et al. [3] concluded from a comprehensive post-earthquake survey that a residual inter-story drift exceeding 0.5% makes demolition a more feasible choice than repair.

Having drawn these lessons, the community of seismic engineers starts to seriously consider residual deformation as a supplementary seismic performance index. An emerging

class of structural systems, namely, self-centering structures, have received extensive research interests [4-14]. Primary lateral load resistant members such as beam-to-column connections and braces are endowed with self-centering capability which is commonly provided by the post-tension (PT) technology. As a result, a typical flag-shaped hysteretic behavior is developed which naturally eliminates residual deformation. However, many follow-up studies revealed that the self-centering capability is achieved at the cost of undesirable structural responses. Firstly, the peak deformation response of self-centering structures is indeed amplified compared with conventional structures due to the decreased energy dissipation capacity [15-16]. The excessively large peak deformation not only increases the risk of collapse, but also causes significant damage to the facades, pipelines and other drift-sensitive systems, making repair work very difficult. Secondly, high-mode effect is pronounced in self-centering structures, and this leads to further increases in the inter-story drift at upper floors. It was confirmed that the high-mode effect is also related to the insufficient energy dissipation capacity of the self-centering structures [17]. Thirdly, the peak absolute floor acceleration, which is responsible for most non-structural damages, is much larger in self-centering structures than conventional yielding systems [15, 18]. It is reminded that injuries, repair costs, business interruption and even fatalities related to non-structural failure far exceeded those related to structural failures in most of the past earthquakes [19-21]. Finally, self-centering members, especially braces, have limited ductility due to the limited elastic strain of the PT tendons [12-14]. The loss of stiffness and strength due to the yielding or even failure of the PT tendons would put the structure in great danger during the mainshock and aftershocks.

Several improvements to the existing self-centering design concept have been recently proposed in order to address some, if not all the above issues. For example, smart materials such as shape memory alloys (SMAs) [22-33] have been considered to provide significantly

increased ductility and extra energy dissipation thanks to the superelastic effect. Moreover, Kam et al. [34] and Tzimas et al. [35] suggested to use various energy dissipation devices such as metallic or viscous dampers in self-centering moment resisting frames with PT-based self-centering connections. A common finding was that these additional energy dissipation sources effectively control the peak deformation and floor acceleration responses. One challenge, however, is that these self-centering connections rely on the gap opening mechanism which causes a detrimental "beam-growth effect", resulting in significant slab damage and incompatibility of structural deformation; therefore, special treatments on the connections or flooring system are necessary [36-40]. Silwal et al. [41-42] proposed superelastic viscous dampers for enhancing the seismic performance of steel moment frames. Kitayama and Constantinou [43] developed a new fluidic self-centering system which offers benefits of reduction in various seismic demand indices. These dampers leveraged the self-centering capability of SMA cables or helical springs and supplementary energy dissipation provided by either viscoelastic materials or fluid viscous dampers.

With initial confidence gained from these pioneering investigations, the present study sheds further light on the potential of "hybrid" self-centering solutions for improved seismic performance. The following objectives are particularly pursued: 1) a more practical hybrid self-centering member design is desirable, preferably having the benefits of high commercialization value, fast installation (elimination of field pre-tensioning), sufficient ductility, integrated function, and free from repair after major earthquakes; 2) the rationale behind the unique dynamic responses of the hybrid systems needs to be further explained; 3) the sensitivity of the structures to special frequency characteristics of ground motions, i.e., pulse-like near-fault earthquakes, should be understood, and the influences of key structural design parameters, such as base shear, supplemental damping ratio and supplementary damper arrangement, on the performances of the structures under various earthquake types should be

revealed; 4) a reliable residual deformation prediction model has yet to be available. The relationship between the residual and peak deformations of hybrid self-centering structures should be quantified.

In the following discussions, two novel hybrid self-centering braces incorporating prestressed superelastic SMA elements and integrated viscoelastic damper (VEDs) are proposed, with the working principle presented in detail. Subsequently, seven basic prototype buildings, including a conventional buckling-restrained braced frame (BRBF), a "pure" self-centering braced frame (SCBF), and five hybrid self-centering steel braced frames (HBFs) with different base shears and supplemental damping arrangements, are designed according to ASCE 7-16 [44]. These structures are then evaluated in terms of the peak/residual inter-story drift and peak floor acceleration demands with selected far-field and near-fault ground motions. The influence of the varying brace parameters on the key seismic demands is further discussed, and the reasons behind the observed trends are explained. Based on the available data, preliminary design recommendations for the proposed hybrid structures are provided, and a probability-based model for residual inter-story drift prediction is finally developed.

2. Basic concepts of SMA-viscoelastic hybrid braces

2.1 Information of SMA and viscoelastic materials

SMA is a unique class of metal capable of recovering a large strain of up to 10% at its austenite state. The entire recovery process is spontaneous at room temperature with no external heat/power required. This phenomenon is called superelastic effect, which makes SMA an ideal candidate for self-centering braces due to the large deformability (much larger than normal steel tendons) and supplemental energy dissipation. The typical uniaxial stress-strain relationship of the SMA material is shown in Fig. 1(a), where the basic mechanical parameters such as the transformation start and finish stresses (σ_{Ms}, σ_{As}, σ_{Mf} and σ_{Af}) are

marked in the figure. In practice, SMAs can be produced into various forms such as monofilament wires, cables, bars as well as different types of springs [45]. In this study, two types of hybrid brace are conceptually proposed, one with SMA cables and the other one with SMA ring springs. The superior performance of both SMA element types have been experimentally verified by the authors and co-workers. For example, Fig. 2(a) shows the test setup and typical result of a 7×19×1.0 SMA cable under cyclic loading, where satisfactory performance is observed. More details can be found in [46-49].

On the other hand, viscoelastic materials have been applied in the aircraft, aerospace, and construction industries for decades [50]. Viscoelastic materials are rate sensitive and act via shear deformation between two steel plates. The output force F_{ve} can be expressed by:

$$F_{ve} = K_{eff} u + C_e (v)^{\alpha} \tag{1}$$

$$K_{eff} = \frac{nG^{'}A}{h},\ C_e = \frac{nG^{''}A}{\omega h} \tag{2}$$

where K_{eff} is the equivalent storage stiffness which is determined by the number of viscoelastic material layers (n), storage modulus (G'), area of viscoelastic material (A), and thickness of a single viscoelastic layer (h); u is the displacement, v is the velocity; C_e is the equivalent damping coefficient, in which G'' is the loss modulus and ω is the circular frequency; and α is the velocity exponent. Viscoelastic dampers (VEDs) are relatively mature energy dissipation systems, and the available test data are abundant. The typical results conducted by the authors as well as other researchers (e.g., Zimmer [51]) are shown in Fig. 2(b), noting that the hysteresis varies with different compositions. Given that the work done by Zimmer [51] has been widely used, the associated parameters were adopted in the present study for consistency with other independent researchers. The numerical modelling approach considered in this study can well capture the fundamental behavior of different types of VED,

as shown in Fig. 2(b).

Apart from the increased energy dissipation, one motivation behind the combination of SMA and viscoelastic materials is the extra restoring force (i.e., the presence of K_{eff}) provided by the latter which promotes increased self-centering tendency. Moreover, compared with displacement-dependent dampers such as friction and metallic devices, viscoelastic material boosts significant energy dissipation under dynamic (high frequency) excitations whilst providing reduced force under low-frequency loading. Intuitively, this rate-sensitive behavior enables less significant impediment to the self-centering tendency during the shake down process, and therefore the residual deformation could be more efficiently controlled. These are confirmed later in the system-level analysis section.

2.2 Hybrid brace with SMA cables

This type of brace consists of an outer tube, an inner tube, a series of prestressed SMA cables, VEDs, and other necessary accessories such as end-plates, angles, connection plates and position holders, as shown in Fig. 3(a). The brace provides both tensile and compressive deformations, with the SMA cables being always stretched. The SMA cables should be prestressed between the two end-plates in order to provide sufficient “yield” strength and enhanced self-centering capability. As SMA cables have very large recoverable strain, they may not be used along the full length of the brace. In this case, the SMA cables and the extended part (e.g., steel cables) can be connected via couplers.

The working principle of the brace is demonstrated in Fig. 3(b). Assuming that the right end of the brace is fixed (see orientation in the figure), the left connection plate together with the inner tube moves leftwards when the brace is in tension, and this action pushes the left end-plate to move. The right end-plate is constrained by the outer tube and therefore cannot be moved. Such a separation of the two end-plates elongates the SMA cables. When the brace is in compression, the inner tube moves rightwards together with the right end-plate;

however, the left end-plate is constrained by the outer tube, and such a separation of the two end-plates again elongates the SMA cables. The SMA cables work in parallel with the viscoelastic dampers which provide extra energy dissipation via shear deformation. The external plates of the VED are connected to the outer tube via angles, and the middle plate passes through the slotted hole of the outer tube and is inserted into the VED slot which is welded to the inner tube.

To further describe the basic behavior of the brace, the initial deformation and force of the outer and inner tubes after cable prestressing can be expressed by:

$$\delta = \frac{P_f}{k_{ot} + k_{in}}, P_{ot} = \frac{P_f k_{ot}}{k_{ot} + k_{in}}, P_{in} = \frac{P_f k_{in}}{k_{ot} + k_{in}} \tag{3}$$

where P_f is the total cable preload, δ is the deformation of both tubes, P_{in} and P_{ot} are the axial force of the inner and outer tubes, respectively, k_{in} and k_{ot} are the elastic axial stiffness of the inner and outer tubes, respectively. The activation/decompression force P_a can be expressed by:

$$P_a = \frac{P_a}{k_{br}} \cdot k_2 + P_f \tag{4}$$

where k_2 is the "post-yield" stiffness, i.e., that of the forward transformation plateau, as marked in Fig. 1(a), k_{br} is the initial stiffness of the brace prior to activation:

$$k_{br} = k_{ot} + k_{in} + k_2 \tag{5}$$

and therefore,

$$P_a \left(1 - \frac{k_2}{k_{br}}\right) = P_f \tag{6}$$

For most cases $k_{br} >> k_2$, so one can consider:

$$P_a \approx P_f \text{ and } \delta_a = \frac{P_f}{k_{br}} \tag{7}$$

It should be noted that under static loading, the VED has no relative deformation before activation and therefore does not contribute to the load resistance. When the brace is subjected to dynamic excitations, however, the extra force provided by the VED should be taken into account:

$$P_{vf} = C_e \left(f'(t) \right)^{\alpha} \tag{8}$$

where t is time. Therefore, the total brace force upon activation P_{BR} is:

$$P_{SMA} = P_f, P_{VED} = P_{vf} = C_e \left(f'(t) \right)^{\alpha}, P_{BR} = P_f + C_e \left(f'(t) \right)^{\alpha} \tag{9}$$

After the activation, the brace force at any deformation can be described with a similar expression, and it depends on the loading rate/loading frequency, as illustrated in Fig. 1(b).

2.3 Hybrid brace with SMA ring springs

An alternative type of hybrid brace is that incorporating SMA ring springs, as shown in Fig. 4(a). An SMA ring spring group includes a series of inner high-strength steel (HSS) rings and outer SMA rings stacked in alternation with mating taper faces. It resists compressive load by expanding the outer rings (the HSS inner rings are designed to be sufficiently strong). This wedging action together with the friction over the taper interface can provide a very large load resistance and remarkable energy dissipation. The compressive deformation of the ring spring group is recovered due to the superelastic behavior of the SMA when the external load is removed.

The SMA ring springs are housed by the hybrid brace and work together with the VED. The main parts of the brace include an outer tube, a central positioning rod, connection rods, connection plate, sleeve tubes and shim plates, as shown in the figure. The SMA ring springs are first precompressed and confined by the two shim plates, the latter are placed between the ring springs and the connection rods. The connection rods and the central positioning rod are connected by threaded junctions, and the precompression to the SMA ring

springs can be applied by screwing the connection rods or via other feasible ways. The outer tube and sleeve tubes are then assembled via bolted connections, and the external plates and middle plate of each VED are connected to the sleeve tube and extended connection rod, respectively.

Again, assuming that the right end of the brace is fixed when the brace is in tension, as illustrated in Fig. 4(b), the left, central, and right rods move leftwards together, which pushes the right shim plate to compress the SMA ring springs as the left shim plate is constrained by the left sleeve tube. Similarly, when the rods move rightwards, the SMA ring springs are compressed again due to the rightward movement of one shim plate while the other shim plate is constrained. The relative movement between the sleeve tubes and connection rods causes shear deformation of the VEDs. The behavior of the brace under different loading frequencies is expected to be similar to that presented in Fig. 1(b), where a detailed description of the mechanism of the SMA ring springs can be found elsewhere [48]. Experimental verification of the braces will be reserved for future studies.

3. Prototype buildings

3.1 Design and modelling of BRBF

The 9-story BRBF with an inverted-V BRB configuration is designed as an office building located on a stiff soil site (Site Class D) in Los Angeles, as shown in Fig. 5. The present study focuses on a 2D frame that represents half of the structure in the north-south (NS) direction. Rigid beam-to-column connections are assumed for the boundary frame. Therefore, the structure is a dual system where the seismic force is concurrently resisted by the boundary frame and the BRBs. Although simple connections have been gaining popularity for BRBFs for more economical design, the selection of the dual system here is to enable consistency with later discussed SCBF which has not been codified and hence requires certain

redundancy. The BRBF is first designed using the modal response spectrum analysis method, considering the following design response spectral values: $S_{MS} = 3/2S_{DS} = 2.064$g and $S_{M1} = 3/2S_{D1} = 1.061$g. Other basic design parameters include importance factor $I_e = 1.0$, response modification coefficient $R = 8.0$, and deflection amplification factor $C_d = 5.0$. Following the static design, nonlinear response history analysis employing 11 ground motions compatible with the design spectrum is performed to confirm that the ASCE 7-16 drift limits are satisfied under both the design based earthquake (DBE) and maximum considered earthquake (MCE) levels. The detailed design of the BRBs for the different floors is provided in Fig. 5.

The BRBF is modelled and analyzed in the nonlinear dynamic analysis program OpenSees [52]. A basic centerline model is established, and the boundary frame members are simulated by nonlinear beam-column elements using the Steel01 material with idealized kinematic hardening. The BRBs are modelled with “truss” elements using the Steel02 Giuffre-Menegotto-Pinto material model considering isotropic strain hardening. The seismic weight is appropriately distributed to the main frame and the adjacent lean columns, with the P-Δ effect fully considered. A Rayleigh damping with 5% damping ratio for the first and third modes of vibration is adopted. The static pushover curve of the BRBF is shown in Fig. 6.

3.2 Design and modelling of SCBF

The SCBF refers to the structure employing SMA-based self-centering braces (SCBs) in the absence of viscoelastic materials. While different SMA elements can be used for the SCBs, as mentioned in the previous section, the SMA cable solution is selected for the present study. SMA cables have the following advantages compared with other SMA elements: 1) SMA cables are made from monofilament SMA wires, where the latter is the most cost-effective form of SMA products. With a proper cable construction, SMA cables can have basic properties comparable to SMA wires, with stiffness and strength better meeting the practical

demand. 2) Unlike SMA bars, SMA cables are buckling free, easy to handle and spool, and do not need extra heat treatment. 3) SMA cables are highly ductile, reliable, and robust. They typically fail in successive rupture of the wires [49], so the failure process is not radical and is less sensitive to initial imperfections. 4) Diverse helix angles and layups can be adopted for SMA cable productions, which enables flexible properties catering to different requirements.

The SCBF and BRBF share the same boundary frame, and have the same base shear level (V) and fundamental period of vibration (T_1). In other words, the SCBs and BRBs (at the same floor level) are designed to have similar yield resistance and initial stiffness, so they mainly differ in the energy dissipation characteristic. It is noted that the yield resistance of the SCB is determined by the preload applied to the SMA cables, whereas that of the BRB is related to the yielding of the steel core. There are two reasons for assuming the same initial stiffness of the SCB and BRB. Firstly, the actual initial stiffness of a SCB before activation (decompression) of the prestressed SMA cables is subjected to uncertainties related to manufacturing, fabrication, and machining tolerance [9-11, 53]. Huang et al. [54] concluded that the initial stiffness of self-centering members is difficult to predict using theoretical equations because of these uncertainties. Nevertheless, the existing experimental study revealed that the actually measured initial stiffness of SCB specimens are indeed comparable to those of the BRBs with a similar level of load carrying capacity [9-11]. Secondly, by assuming the same initial stiffness, the behavior of the SCBF and BRBF is minimally affected by the varied natural periods, and therefore the influence of the different energy dissipation provided by the two types of braces can be better revealed. The detailing of the SCB is consistent with that presented in Section 2.2, and the basic design information, including the number, length and total preload of the SMA cables, is given in Table 1. The typical 7×19×1.2mm cable construction is considered for the SMA cables, and the preload level corresponds to the “yield” strength of the cables. The effective length of the SMA cables is

preliminarily determined such that a 10% cable strain corresponds to around 5% inter-story drift.

The SCB is modelled in OpenSees using “truss” elements with a modified ‘SelfCentering’ material that captures the flag-shaped hysteresis of the braces. The key parameters for capturing the basic stress-strain behavior of the SMA cable are determined from the existing test results [49], as shown in Fig. 1(a). The stress-strain response is then converted to the load-deformation response of the brace. An energy dissipation factor β of 0.6 is assumed which is typical for SMA cables [49, 55-56].

3.3 Design and modelling of HBF

Five HBFs with combined SMA and viscoelastic materials are designed with variations in base shear (1.0V and 0.75V), added damping ratio (0.1 and 0.2) and height-wise arrangement of the VEDs (uniform and nonuniform distributions). The basic information of the prototype buildings is summarized in Table 2. ASCE 7-16 allows a 25% reduction in the base shear for damped structures; therefore, the 0.75V-series HBFs are those with an approximately 25% reduction in the overall strength of the structure. The modified SMA cable design is provided in Table 1, and the reduced boundary frame is shown in Fig. 7. On the other hand, the 1.0V-series HBFs have the same boundary frame and brace strength as the BRBF/SCBF, so they represent a class of “high-performance” structures and are expected to exhibit enhanced seismic performance than the basic code requirement, although being more expensive.

The first-modal added damping ratio ξ_{add} provided by the viscoelastic material is given by [44]:

$$\xi_{add} = \left(\frac{T_1}{4\pi}\right) \frac{\sum_{j=1}^{M} C_j \cos^2 \theta_j \phi_{rj}^2}{\sum_{i=1}^{N} \frac{w_i}{g} \phi_{im}^2} \tag{10}$$

where C_j is the viscous damping coefficient of the jth viscoelastic damper at the considered floor level, θ_j is the diagonal angle of the brace, ϕ_{rj} is the relative modal displacement at the considered floor level, N is the total floor number, w_i is the seismic weight of the ith floor, ϕ_{im} is the mth modal displacement at the ith level. Linear viscoelastic materials are considered (velocity exponent α = 1.0), and the basic material properties are obtained from the test done by Zimmer [51], i.e., storage modulus G' = 0.9 MPa and loss modulus G'' = 1.22 MPa. The thickness of each layer is 30 mm, and a total of eight layers are considered for each brace. Except for HBF-0.75V-0.1U where the same amount of viscoelastic material is used throughout all the floors, the output force of the VEDs (considering a consistent loading frequency of 1Hz) is proportional to the strength of the SCB at the same floor for the remaining four HBFs. The detailed design of the VEDs for the different buildings is summarized in Table 3. In OpenSees, the VED is simulated by two paralleled spring elements with Viscous and Elastic material properties. This model is also called Kelvin-Voigt model [50].

4. Ground motions and structural performance

4.1 Ground motions

A total of 20 far-field (FF) and 20 pulse-like near-fault (NF) ground motions at the MCE level are considered in the analysis. The FF records are selected from the FEMA P695 database [57] and are scaled to fit the target spectrum, as shown in Fig. 8(a). For pulse-like NF records, the criteria proposed by Baker [58] are used during the selection process. Baker's criteria contain three conditions. Firstly, the pulse indicator (PI), as defined in Eq. (4), should not be

less than 0.85. This indicator is related to the PGV (peak ground velocity) and the energy of both the original ground motion and the "residual ground motion" after "extracting" the pulse. The PGV and energy ratios are defined in Eq. (5), noting that the energy can be calculated as the cumulative squared velocity (CSV) of the record. Secondly, pulsing should occur at the beginning of the record, i.e., $t_{20\%,orig}>t_{10\%,pulse}$, where $t_{20\%,orig}$ is the time when 20% of the total CSV of the original ground motion is reached, and $t_{10\%,pulse}$ is the time when 10% of the total CSV of the extracted pulse is reached. Ensuring $t_{20\%,orig}>t_{10\%,pulse}$ means that the velocity pulse starts before a significant portion of energy is observed. The third condition is that the PGV of the selected records should be larger than 30cm/sec.

$$PI = (1+e^{-23.3+14.6(PGVRatio)+20.5(EnergyRatio)})^{-1} \tag{11}$$

$$PGVRatio = \frac{PGV_{residual}}{PGV_{original}}, EnergyRatio = \frac{\int_0^t V^2(t)dt_{residual}}{\int_0^t V^2(t)dt_{original}} \tag{12}$$

Unlike FF records which are readily scalable, scaling should be more cautiously done for NF ground motions where the key pulsing characteristics may be violated by uniform scaling [59]. Therefore, in this study, the 20 NF ground motions are unscaled, which are carefully selected to match the design spectrum, as shown in Fig. 8(b). It is confirmed that the mean spectrum of the NF records is not less than the design response spectrum for periods ranging from $0.2T_1$ to $2.0T_1$, which satisfies the ASCE 7-16 requirements. The details of the 40 ground motions, including the earthquake name, magnitude, PGA, PGV, etc., can be found elsewhere [60].

4.2 Peak inter-story drift (PID)

The mean height-wise peak inter-story drift (PID) distributions of the considered structures under the two types of earthquakes are shown in Fig. 9(a), and the maximum mean PIDs

(among all the floor levels) of the structures are summarized in Table 2. Keeping the record-to-record (RTR) variability in mind, the mean responses are discussed hereafter unless stated otherwise. The results show that the maximum PID of the SCBF in the absence of the viscoelastic material is on average 21% larger than that of the BRBF. In addition, because of the high-mode effect, the difference in the PID between the two structures is more significant at the upper floors. High-mode effect is highly coupled with the fundamental mode of vibration of SCBFs and hence causes enlarged deformation responses concentrated at upper floors [17].

The use of the viscoelastic material is highly effective in PID control for the self-centering structures under both earthquake types. With an added damping ratio of 0.1, the maximum PID of the HBF without strength reduction (1.0V) is decreased by more than 40%. The effectiveness still holds when the base shear is reduced, where the maximum PID of HBF-0.75V-0.1 is decreased by approximately 35% compared with the SCBF. It is believed that the decrease in PID mainly results from the increase in the energy dissipation capacity provided by the viscoelastic material. Increasing the added damping ratio from 0.1 to 0.2 brings certain but less significant further benefits. The above observations indicate that a cost effective self-centering solution, i.e., reduced boundary frame with less SMA consumption, can be realized by introducing only a small amount of viscoelastic materials for energy dissipation. A uniform distribution of the viscoelastic materials (i.e., HBF-0.75V-0.1U) leads to changes in the height-wise PID distribution, although the maximum PID is not significantly affected. Another encouraging finding is that the maximum PID of all the HBFs is smaller than that of the BRBF, which reaffirms the superiority of the hybrid energy dissipation strategy.

4.3 Residual inter-story drift (RID)

The residual inter-story drifts (RIDs) of the structures are shown in Fig. 9(b), and the key

results are summarized in Table 2. Clearly, the BRBF exhibits the largest RID because of the full hysteretic behavior of the brace. The mean maximum RIDs of the BRBF under the FF and NF earthquakes are 0.49% and 1.25%, respectively. It is reminded that four damage states (DS) are stipulated in FEMA P-58 [61]: DS1, the strictest class, requires a 0.2% RID limit to eliminate the necessary structural realignment, although adjustment and repairs to non-structural components may be required; DS2 has a 0.5% RID limit to ensure economically feasible structural repairs with limited degradation in structural stability; DS3 with a RID limit of 1% indicates that major structural repair work is needed to keep the structure safe, although the effort can be economically and practically infeasible; DS4, where the RID exceeds 1.0%, means an excessive residual deformation which puts the structure in danger of collapse from aftershocks. According to these definitions, the BRBF has an average RID response which may allow economically feasible structural repairs under the FF earthquakes, but loses the possibility of repair under the NF earthquakes. The enlarged RID caused by the NF ground motions (increased by 160% compared with the case of FF earthquakes) is due to the large excursion induced after the dominant ground velocity pulse.

As anticipated, the SCBF exhibits much reduced RID responses. The mean RID under the FF earthquakes is 0.114%, and due to the pulsing effect, the value under the NF earthquakes is increased and slightly exceeds the DS1 limit. The RID of the SCBF is mainly caused by the inelastic deformation of the boundary frame, recalling that a dual system is adopted. The RID is further suppressed when the structure has an added damping ratio of 0.1 contributed by the viscoelastic material (i.e., HBF-1.0V-0.1). It is believed that the decrease in RID directly results from the remarkable decrease in the PID response, as discussed in Section 4.2. Maintaining the same added damping ratio, the RID is not very sensitive to the base shear. This is consistent with the findings by previous researchers working on conventional systems [20, 62]. Compared with the BRBF and SCBF, the HBF seems to exhibit more

uniform height-wise distributions of RID, and in addition, the RID is more effectively controlled by using the same amount of viscoelastic materials for the different floors.

A counterintuitive finding is that further increasing the added damping ratio from 0.1 to 0.2 causes a pronounced regain of the RID, even though the PID is further decreased. For example, as shown in Table 2, the mean maximum RID of HBF-1.0V-0.2 under the FF and NF earthquakes is increased by 82% and 149%, respectively, compared with HBF-1.0V-0.1. This indicates that an overly large added damping ratio is detrimental to the recoverability of the hybrid structures, especially under NF earthquakes. The influence of the added damping ratio is more clearly illustrated via the dynamic shake-down responses of the structures subjected to a typical pulse-like NF earthquake excitation, as shown in Fig. 10(a). The HBF-1.0V-0.1 and HBF-1.0V-0.2 display a similar PID, which is smaller than that of the SCBF. When returning from the PID towards the upright position, the reversed path of HBF-1.0V-0.2 is “shortened”, leading to an enlarged permanent excursion and finally a larger RID during the subsequent shake down.

The enlarged RID can be explained from several perspectives. Fig. 10(b) shows the force-deformation history of typical braces at the considered floor level, highlighting the first half cycle immediately following the PID. Clearly, due to the increased damping, the magnitude of the negative force is increased, which means that the barrier against the self-centering tendency rises when the structure tries to move towards the upright position. As the RID is largely related to the inelastic deformation of the boundary frame, when more energy is dissipated by the viscoelastic material, the strain energy stored in the boundary frame at the new rest position is decreased, which means that the residual deformation is increased [63]. This phenomenon can be illustrated by an idealized unloading path of the boundary frame, as shown in Fig. 10(c), where the difference in the strain energy is the area of the shaded parallelogram which increases with increasing viscoelastic damping. Due to the extra

damping, the residual deformation increases from Δ_r to $\Delta_{r,ve}$. Furthermore, when more viscoelastic materials are used, the load resistance of the brace increases, so does the force demand of the boundary frame members. This also explains the increased RID of HBF-1.0V-0.2 of which the boundary frame experiences more significant yielding. Generally speaking, most of the HBFs exhibit well-controlled RID responses and satisfy the DS1 limit. The exception is those with 0.2 added damping ratio under NF earthquakes, where the DS1 limit is exceeded.

4.4 Absolute peak floor acceleration (PFA)

Absolute peak floor acceleration (PFA) is closely related to the non-structural failure and injury/fatality caused by an earthquake. The height-wise PFA responses of the structures are shown in Fig. 9(c), and the maximum values are summarized in Table 2. An obvious finding is that the SCBF exhibits much amplified PFA responses than the BRBF. Tremblay et al. [18] concluded that the large PFA is caused by inconsistent inter-story shear forces of the two adjacent floors, where one floor has the shear force lagging that of the neighboring floor during the shaking. The increase in PFA in the SCBF is because of the increased "transition points" of the flag-shaped hysteresis during the unloading and reloading paths compared with the full hysteretic response, and as a result a larger difference in the shear force between the adjacent stories. The more frequent transitions have the possibility of producing a very short duration, high amplitude PFA pulse.

The shortcoming of the SCBF regarding the large PFA response is effectively addressed by the HBF solution. As can be seen in Table 2, the average PFA of the HBFs falls back to the level which is similar to or even smaller than that of the BRBF. The reason behind the observed trend can be explained by tracing the force-deformation paths of the braces at the two adjacent floors. Fig. 11(a) shows the PFA time-histories of a typical floor (i.e., 2nd floor)

of the SCBF and HBF-1.0V-0.1 under the same excitation (NF13). Large PFA responses of the two structures generally occur at the same time, but the amplitudes differ significantly. Three peaks at three different moments are selected, as marked by red circular, blue square, and green triangular dots. The corresponding force-deformation paths of the braces at the adjacent floors (2^{nd} and 3^{rd} floors) are shown in Fig. 12. For the SCBs, transitions occur at one or both floors, which leads to significant changes in the inter-story shear force. On the other hand, the change of the forces of the hybrid braces is gentler because of the velocity-sensitive nature of the viscoelastic materials. At the three particular moments, the changing tendency and changing rate of the adjacent floors is similar. This causes mild changes of the difference of the inter-story shear, and therefore large PFA pulses are less likely to be triggered. Fig. 11(b) confirms that the difference of the brace forces between the adjacent floors for the HBF is smaller than the SCBF at these critical moments.

The results also show that an added damping ratio of 0.1 is adequately effective for PFA mitigation, while an increased damping of 0.2 brings limited extra benefit. In addition, a reduction in base shear tends to decrease the PFA response, which echoes the existing studies showing that a more pronounced inelastic behavior due to reduced strength decreases the acceleration demands [19]. Furthermore, for all the considered structures, the FF and NF ground motions lead to similar PFA magnitudes, indicating that the PFA is not sensitive to the pulsing effects of the ground motion.

5. Further discussions

5.1 Parametric study

After understanding the fundamental behavior of the prototype buildings, the influence of an extended range of brace parameters is revealed. The first part of the parametric study is based on the 0.75V frame and focuses on two key parameters, namely, energy dissipation factor β

(defined in Fig 1) and added damping ratio ξ_{add}, of the hybrid braces. Three energy dissipation factors, i.e., β = 0.6 (reference case for prototype buildings), 1.0, and 1.5, are used to consider the possible varied design of the self-centering components of the brace. Especially, β = 1.5 represents a "partial self-centering" behavior where increased energy dissipation is provided (e.g., by extra friction or metal yielding mechanisms) compared with a typical fully self-centered response. The study also covers five levels of added damping ratio, i.e., ξ_{add} = 0.0, 0.05, 0.1, 0.15, and 0.2, where ξ_{add} = 0.0 represents a pure SCBF in the absence of the viscoelastic material. The same suites of FF and NF ground motions are employed for the parametric study.

The variations of the critical seismic performances with β and ξ_{add} are shown in Figs. 13 and 14, respectively. The results confirm that the NF earthquakes consistently cause increased PID and RID responses compared with the FF earthquakes. An increase in β tends to mitigate the PID, and this trend is more obvious for the SCBF with ξ_{add} = 0. Increasing β from 0.6 to 1.0 could slightly decrease the RID because of the decreased PID; however, the RID rises again when β increases further from 1.0 to 1.5. This is not surprising, as the partial self-centering behavior of the brace causes decreased self-centering capability. An increase in β also effectively decreases the PFA response of the SCBF with ξ_{add} = 0. Generally speaking, the PID, RID and PFA responses of the SCBF with ξ_{add} = 0 are more sensitive to β compared with the case of ξ_{add} = 0.1, because the former lacks the additional adaptive mechanism offered by the viscoelastic material. In other words, the hybrid solution provides reliable and consistent structural control capabilities, and the effectiveness is not very sensitive to the hysteretic properties of the braces.

As shown in Fig. 14, increasing the ξ_{add} decreases the PID, and such trend is most obvious when ξ_{add} increases from 0.0 to 0.05. Interestingly, ξ_{add} = 0.05 concurrently leads to

the smallest RID. The reason behind the detrimental effect of a large ξ_{add} has been explained previously. The PFA response is also effectively suppressed when ξ_{add} increases from 0.0 to 0.05, while limited further efficiency is gained when ξ_{add} increases beyond 0.1. The above phenomena indicate that ξ_{add} = 0.05 leads to a well-balanced control of the PID, RID and PFA responses. An overly large added damping ratio is unnecessary for the considered structures, and this conclusion is important for encouraging more economical design of the proposed HBFs.

For completeness of the study, the second part of the parametric study focuses on the influence of base shear on the frame response as well as the applicability of the hybrid solution to the BRBFs. An additional 0.5V HBF, i.e., model HBF-0.5V-0.1, is designed and compared with the existing models, as shown in Fig. 15. It is of interest to find that even the base shear is further decreased to 0.5V, the structural performance is not evidently inferior to that of the 0.75V and 1.0V structures. In particular, the RID is not affected, and the PFA is further decreased with decreasing base shear. The results indicate that the presence of VED causes less sensitivity of the structure to the base shear, and the codified 25% maximum reduction limit in strength could be on the conservative side and may be further relaxed for the proposed hybrid self-centering systems.

Finally, two more structures which combine BRB with VED, i.e., models HBRBF-1.0V-0.1 and HBRBF-0.75V-0.1, are considered. The results in Fig. 15 show that the combination of BRB and VED leads to positive outcomes. The PID is decreased under both FF and NF earthquakes, which is majorly because of the enhanced energy dissipation capacity. The RID is also effectively reduced (although still larger than that of the hybrid self-centering structures), which is attributed to the restoring action and the increased post-yield stiffness provided by the VEDs. It is also encouraging to observe that the PFA is further mitigated in the presence of the VED. Compared with HBRBF-1.0V-0.1, a 25% reduction in

the base shear (HBRBF-0.75V-0.1) leads to equally satisfactory performances. From the above results, one may preliminarily conclude that the hybrid solution is also applicable to BRBFs.

5.2 Resilience assessment based on RID prediction

RID is recognized as a critical performance index for structural resilience assessment. Given that the drift limit (i.e., allowed PID) is often clearly stated in the design standards, say, 2% under the DBE and 4% under the MCE, designers are particularly interested in knowing the relationship between the PID and RID responses, which enables a quick evaluation of the damage state class (e.g., DS1~DS4) of the designed building according to the estimated PID. The statistical link between the two quantities is also useful when one wants to determine the PID limit based on a permissible RID level (e.g. 0.2% for DS1) required by the owners and other stakeholders.

For any inelastic system, the possible residual deformation Δ_r during dynamic shake down is always smaller than the maximum transient deformation Δ_{max} minus the elastic deformation Δ_{el}. In other words, Δ_{max}-Δ_{el} is an upper bound for the possible residual deformation, and therefore a normalized residual deformation factor R_r, which ranges between 0.0 and 1.0, could be a convenient index for describing the link between RID and PID:

$$R_r = \frac{\Delta_r}{\Delta_{max} - \Delta_{el}} \tag{13}$$

For the considered braced frames, the elastic inter-story drift is on average 0.25% according to the pushover response.

Although different structural types have different self-centering capabilities and even the same structure could exhibit a highly diverse R_r values under different earthquakes, an important finding from the present study is that the R_r tends to follow a lognormal distribution

when subjected to the RTR viability, as typically shown in Fig. 16. Accordingly, the probability density function $y(R_r)$ and cumulative distribution function $P(R_r)$ can be expressed by:

$$y(R_r) = \frac{1}{R_r \sigma \sqrt{2\pi}} \exp\left[\frac{-\left(\log R_r - \mu\right)^2}{2\sigma^2}\right] \tag{14}$$

$$P(R_r) = \frac{1}{\sigma \sqrt{2\pi}} \int_0^{R_r} \frac{1}{t} \exp\left[\frac{-\left(\log t - \mu\right)^2}{2\sigma^2}\right] dt \tag{15}$$

The cumulative distribution curves of the seven prototype buildings under the FF and NF earthquakes are compared in Fig. 17(a), and the logarithmic mean (μ) and standard deviation (σ) are given in Table 4. Engineers are free to choose the desired R_r values with a certain probability of exceedance in practical design. For example, under the NF earthquakes, the median R_r of the BRBF is approximately 0.37, which means that the RID is expected to be 37% of the inelastic PID. In order to have a more conservative estimation, engineers could alternatively use the 84th percentile R_r value, which is around 0.6. As expected, the R_r values of the SCBF and HBFs are significantly reduced. It is also found that HBF-0.75V-0.1U, which employs uniform viscoelastic materials, consistently lead to the smallest R_r values compared with the other structures.

Similarly, the cumulative distribution curves of the frames with the extended brace parameters are shown in Figs. 17(b) and 17(c). Being in line with the trend revealed previously, a relatively small ξ_{add} (i.e., $\xi_{add} \leq 0.1$) consistently reduces the R_r value compared with the pure SCBF. When $\xi_{add} \geq 0.15$, the R_r value is decreased at low percentile levels, but an opposite trend is shown at high percentile levels. The "flatter" slope of the cumulative distribution curve of the highly damped HBFs indicates a wider distribution of the R_r value and hence less predictable RID response. The R_r value increases with an increase in

the energy dissipation factor of the brace, and this trend is especially obvious when β increases from 1.0 to 1.5. This is due to the more evident increase in the RID and simultaneously the decrease in the PID when β exceeds 1.0. For the two different earthquake types, the NF ground motions cause a more remarkable diversity in the cumulative distribution curves. This is because the structures undergo more significant inelastic behavior under pulse-like excitations, resulting in increased uncertainty of the RID response.

Regarding the design application, although the cumulative distribution curves presented in Fig. 17 may not be appliable to all types of structures, the obtained tendencies are indeed representative of the typical code-compliant multi-story braced frames in practice. More importantly, the proposed assessment approach can be easily extended to other structures. Engineers may select an appropriate R_r value with a required probability of exceedance to quickly understand the relationship between the RID and PID for the proposed HBFs, at least during preliminary design stages. Fig. 18 shows a possible design chart (together with the recorded data) converted from Fig. 17 for representative HBFs, where the RID could be quickly obtained from the PID, and vice versa.

6. Summary and conclusions

This study has shed considerable light on the application of SMA-viscoelastic hybrid braces for seismic resilience. The main attraction of the proposed HBF is the effective control of the RID without necessarily compromising other seismic performances. The study commenced with the introduction of two conceptual hybrid self-centering braces incorporating prestressed superelastic SMA elements and integrated VEDs. The detailed design and working principle were discussed. Subsequently, a system-level analysis on seven prototype buildings, including a BRBF, a SCBF and five HBFs, was carried out. This was followed by a parametric study considering an extended range of brace parameters. A

probability-based RID prediction methodology was finally proposed. The main findings and conclusions are summarized as follows.

- The pure SCBF has larger PID response than the BRBF because of the decreased energy dissipation capacity. The detrimental high-mode effect is also responsible for the increased PID of the SCBF, especially at upper floors.
- The use of the viscoelastic material to reach a moderate added damping ratio of 0.1 is highly effective in PID control for self-centering structures under both the FF and NF earthquakes; however, further benefits can hardly be achieved when increasing the added damping ratio from 0.1 to 0.2.
- The SCBF exhibits much reduced RID response than the BRBF. A further decrease in RID is achieved with an added damping ratio of 0.1. However, increasing the added damping ratio from 0.1 to 0.2 causes a pronounced regain of the RID, especially under NF earthquakes. This indicates that an overly large added damping ratio is detrimental to the self-centering capability.
- The SCBF exhibits much amplified PFA responses compared with the BRBF because of the increased number of transition points of the flag-shaped hysteresis. Nevertheless, this shortcoming is effectively addressed by the HBF solution, where the average PFA of the HBFs falls back to the level which is similar to or even smaller than that of the BRBF.
- Based on the limited data from the parametric study, it was concluded that a large added damping ratio is unnecessary for SMA-viscoelastic hybrid solutions; $\xi_{add} = 0.05$ appears to be optimal for simultaneous PID, RID and PFA control. This means that the proposed HBFs can be designed in a cost-effective way.
- The presence of VED leads to less sensitivity to the base shear, where a 50% reduction in strength/base shear could still maintain good seismic performance for the proposed

hybrid self-centering systems. In addition, the hybrid solution is also effective for BRBFs for seismic control.

- A normalized residual deformation factor R_r was proposed for describing the statistical link between the RID and PID. The R_r follows a lognormal distribution for the considered structures. A series of cumulative distribution curves are provided, from which engineers could select an appropriate R_r value with a certain probability of exceedance to conduct seismic resilience assessments.

7. Acknowledgements

The financial supports from the National Natural Science Foundation of China (NSFC) with Grant Nos. 51778456, 52078359, 51820105013 and 51778459 are gratefully acknowledged. Supports for this study were also provided by the Chinese National Engineering Research Centre for Steel Construction (Hong Kong Branch).

8. References

[1] Kawashima, K., MacRae, G. A., Hoshikuma, J., and Nagaya, K. 1998. Residual displacement response spectrum. *Journal of Structural Engineering* 124(5): 523-530. doi: 10.1061/(ASCE)0733-9445(1998)124:5(523).

[2] Wood A, Noy I, Parker M. 2016. The Canterbury rebuild five years on from the Christchurch earthquake. *Reserve Bank of New Zealand Bulletin* 79(3):1–16.

[3] McCormick J, Aburano H, Ikenaga M, Nakashima M. 2008. Permissible residual deformation levels for building structures considering both safety and human elements. *Proc. 14th World Conf. Earthquake Engineering*, Seismological Press of China, Beijing.

[4] Ricles JM, Sause R, Garlock M, Zhao C. 2001. Post-tensioned seismic resistant connections for steel frames. *Journal of Structural Engineering* 127(2): 113-21. doi: 10.1061/(ASCE)0733-9445(2001)127:2(113).

[5] Ricles JM, Sause R, Peng SW, Lu LW. 2002. Experimental evaluation of earthquake resistant post-tensioned steel connections. *Journal of Structural Engineering* 128(7): 850-9. doi: 10.1061/(ASCE)0733-9445(2002)128:7(850).

[6] Lin YC, Sause R, Ricles JM. 2013. Seismic performance of a steel self-centering moment resisting frame: hybrid simulations under design basis earthquake. *Journal of Structural Engineering* 139(11): 1823-32. doi: 10.1061/(asce)st.1943-541x.0000745.

[7] Zhang AL, Zhang YX, Li R, Wang ZY. 2016. Cyclic behavior of a prefabricated self-centering beam–column connection with a bolted web friction device. *Engineering Structures* 111: 185-198. doi: 10.1016/j.engstruct.2015.12.025.

[8] Li Z, He M, Wang K. 2018. Hysteretic performance of self-centering glulam beam-to-column connections. *Journal of Structural Engineering* 144(5):04018031. doi: 10.1061/(ASCE)ST.1943-541X.0002012.

[9] Christopoulos C, Tremblay R, Kim HJ, Lacerte M. 2008. Self-centering energy dissipative bracing system for the seismic resistance of structures: development and validation. *Journal of Structural Engineering* 134(1):96-107. doi: 10.1061/(ASCE)0733-9445(2008)134:1(96).

[10] Erochko J, Christopoulos C, Tremblay R. 2015. Design, testing, and detailed component modeling of a high-capacity self-centering energy-dissipative brace. *Journal of Structural Engineering* 141(8): 04014193. doi: 10.1061/(ASCE)ST.1943-541X.0001166.

[11] Erochko J, Christopoulos C, Tremblay R. 2015. Design and testing of an enhanced-elongation telescoping self-centering energy-dissipative brace. *Journal of Structural Engineering* 141(6):04014163. doi: 10.1061/(ASCE)ST.1943-541X.0001109.

[12] Erochko J, Christopoulos C, Tremblay R, Kim HJ. 2013. Shake table testing and numerical simulation of a self-centering energy dissipative braced frame. *Earthquake Engineering & Structural Dynamic* 42(11): 1617–1635. doi: 10.1002/eqe.2290.

[13] Chou CC, Chen YC, Pham DH, Truong VM. 2014. Steel braced frames with dual-core SCBs and sandwiched BRBs: mechanics, modeling and seismic demands. *Engineering Structure* 72:26-40. doi: 10.1016/j.engstruct.2014.04.022.

[14] Chou CC, Wu TH, Beato ARO, Chung PT, Chen YC. 2016. Seismic design and tests of a full-scale one-story one-bay steel frame with a dual-core self-centering brace. *Engineering Structures* 111:435-50. doi: 10.1016/j.engstruct.2015.12.007.

[15] Fang C, Zhong Q, Wang W, Hu S, Qiu C. 2018. Peak and residual responses of steel moment-resisting and braced frames under pulse-like near-fault earthquakes. *Engineering Structures* 177: 579-597. doi: 10.1016/j.engstruct.2018.10.013.

[16] Fan X, Xu L, Li Z. 2019. Seismic performance evaluation of steel frames with pre-pressed spring self-centering braces. *Journal of Constructional Steel Research* 162: 105761. doi: 10.1016/j.jcsr.2019.105761.

[17] Qiu CX, Zhu S. 2016. High-mode effects on seismic performance of multi-story self-centering braced steel frames. *Journal of Constructional Steel Research* 119:133-43. doi: 10.1016/j.jcsr.2015.12.008.

[18] Tremblay R, Lacerte M, Christopoulos C. 2008. Seismic response of multistory buildings with self-centering energy dissipative steel braces. *Journal of Structural Engineering* 134(1):108–20. doi: 10.1061/(ASCE)0733-9445(2008)134:1(108).

[19] Ray-Chaudhuri S, Hutchinson TC. 2011. Effect of nonlinearity of frame buildings on peak horizontal floor acceleration. *Journal of Earthquake Engineering* 15(1):124–42. doi: 10.1080/13632461003668046.

[20] Karavasilis TL, Seo CY. 2011. Seismic structural and non-structural performance evaluation of highly damped self-centering and conventional systems. *Engineering Structures* 33(8): 2248–58. doi: 10.1016/j.engstruct.2011.04.001.

[21] Shu Z, Zhang J, Nagarajaiah S. 2016. Dimensional analysis of inelastic structures with negative stiffness and supplemental damping devices. *Journal of Structural Engineering* 143(3):04016184. doi: 10.1061/(ASCE)ST.1943-541X.0001658.

[22] Fang C, Yam MCH, Lam ACC, Xie LK. 2014. Cyclic performance of extended end-plate connections equipped with shape memory alloy bolts. *Journal of Constructional Steel Research* 94(94):122-36. doi: 10.1016/j.jcsr.2013.11.008.

[23] Qiu C, Li H, Ji K, Hou H, Tian L. 2017. Performance-based plastic design approach for multi-story self-centering concentrically braced frames using sma braces. *Engineering Structures* 153: 628-638. doi: 10.1016/j.engstruct.2017.10.068.

[24] Yam MCH, Fang C, Lam ACC, Zhang YY. 2015. Numerical study and practical design of beam-to-column connections with shape memory alloys. *Journal of Constructional Steel Research* 104:177-92. doi: 10.1016/j.jcsr.2014.10.017.

[25] Wang B, Zhu S, Qiu C, Jin H. 2019. High-performance self-centering steel columns with shape memory alloy bolts: Design procedure and experimental evaluation. *Engineering Structures* 182: 446-458. doi: 10.1016/j.engstruct.2018.12.077.

[26] Wang W, Fang C, Liu J. 2017. Self-centering beam-to-column connections with combined superelastic SMA bolts and steel angles. *Journal of Structural Engineering* 143(2):04016175. doi: 10.1061/(ASCE)ST.1943-541X.0001675.

[27] Fang C, Wang W, He C, Chen YY. 2017. Self-centring behaviour of steel and steel-concrete composite connections equipped with NiTi SMA bolts. *Engineering Structures* 150:390-408. doi: 10.1016/j.engstruct.2017.07.067.

[28] Wang W, Fang C, Yang X, Chen YY, Ricles J, Sause R. 2017. Innovative use of a shape memory alloy ring spring system for self-centering connections. *Engineering Structures* 153:503-15. doi: 10.1016/j.engstruct.2017.10.039.

[29] Miller DJ, Fahnestock LA, Eatherton MR. 2012. Development and experimental validation of a nickel-titanium shape memory alloy self-centering buckling-restrained brace. *Engineering Structures* 40:288-98. doi: 10.1016/j.engstruct.2012.02.037.

[30] Qiu C, Zhu S. 2017. Shake table test and numerical study of self-centering steel frame with SMA braces. *Earthquake Engineering & Structural Dynamic* 46(1):117-37. doi: 10.1002/eqe.2777.

[31] Qiu C, Zhu S. 2017. Performance-based seismic design of self-centering steel frames with SMA-based braces. *Engineering Structures* 130:67-82. doi: 10.1016/j.engstruct.2016.09.051.

[32] Fang C, Zhou XY, Osofero AI, Shu Z, Corradi M. 2016. Superelastic SMA Belleville washers for seismic resisting applications: experimental study and modelling strategy. *Smart Materials and Structures* 25:105013. doi: 10.1088/0964-1726/25/10/105013.

[33] Fang C, Yam MCH, Lam ACC, Zhang YY. 2015. Feasibility study of shape memory alloy ring spring systems for self-centring seismic resisting devices. *Smart Materials and Structures* 24:075024. doi: 10.1088/0964-1726/24/7/075024.

[34] Kam WY, Pampanin S, Palermo A, Carr AJ. 2010. Self-centering structural systems with combination of hysteretic and viscous energy dissipations. *Earthquake Engineering & Structural Dynamics* 39(10):1083-1108. doi: 10.1002/eqe.983.

[35] Tzimas AS, Kamaris GS, Karavasilis TL, Galasso C. 2016. Collapse risk and residual drift performance of steel buildings using post-tensioned MRFs and viscous dampers in near-fault regions. *Bulletin of Earthquake Engineering* 14(6):1643-1662. doi: 10.1007/s10518-016-9898-3

[36] Feng W, Fang C, Wang W. 2019. Behavior and design of top flange-rotated self-centering steel connections equipped with SMA ring spring dampers. *Journal of Constructional Steel Research* 159:315-329. doi: 10.1016/j.jcsr.2019.04.046.

[37] Fang C, Wang W, Feng W. 2019. Experimental and numerical studies on self-centring beam-to-column connections free from frame expansion. *Engineering Structures* 198: 109526. doi: 10.1016/j.engstruct.2019.109526.

[38] Chou CC, Chen JH. 2011. Seismic design and shake table tests of a steel post-tensioned self-centering moment frame with a slab accommodating frame expansion. *Earthquake Engineering & Structural Dynamics* 40(11):1241-61. doi: 10.1002/eqe.1086.

[39] Chou CC, Chen JH. 2011. Development of floor slab for steel post-tensioned self-centering moment frames. *Journal of Constructional Steel Research* 67(10):1621-35. doi: 10.1016/j.jcsr.2011.04.006.

[40] Garlock MEM, Li J. 2008. Steel self-centering moment frames with collector beam floor diaphragms. *Journal of Constructional Steel Research* 64(5):526-538. doi: 10.1016/j.jcsr.2007.10.006

[41] Silwal B, Ozbulut OE, Michael RJ. 2016. Seismic collapse evaluation of steel moment resisting frames with superelastic viscous damper. *Journal of Constructional Steel Research* 126: 26–36. doi: 10.1016/j.jcsr.2016.07.002.

[42] Silwal B, Michael RJ, Ozbulut OE. 2015. A superelastic viscous damper for enhanced seismic performance of steel moment frames. *Engineering Structures* 105:152–164. doi: 10.1016/j.engstruct.2015.10.005.

[43] Kitayama S, Constantinou M C. 2016. Design and analysis of buildings with fluidic self-centering systems. *Journal of Structural Engineering* 142(11): 04016105. doi: 10.1061/(ASCE)ST.1943-541X.0001583.

[44] American Society of Civil Engineers (ASCE). Minimum design loads for buildings and other structures. ASCE/SEI 7-16, Reston, VA., 2016.

[45] Fang C, Wang W. 2020. Shape memory alloys for seismic resilience. Springer. doi: 10.1007/978-981-13-7040-3.

[46] Fang C, Wang W, Ricles J, Yang X, Zhong Q, Sause R, Chen Y. 2018. Application of an innovative SMA ring spring system for self-centering steel frames subject to seismic conditions. *Journal of Structural Engineering* 144(8):04018114. doi: 10.1061/(ASCE)ST.1943-541X.0002127.

[47] Wang W, Fang C, Zhang A, Liu X. 2019. Manufacturing and performance of a novel self-centring damper with shape memory alloy ring springs for seismic resilience. *Structural Control and Health Monitoring* 26(5):e2337. doi: 10.1002/stc.2337.

[48] Fang C, Wang W, Zhang A, Sause R, Ricles J, Chen Y. 2019. Behavior and design of self-centering energy dissipative devices equipped with superelastic SMA ring springs. *Journal of Structural Engineering* 145(10):0409109. doi: 10.1061/(ASCE)ST.1943-541X.0002414.

[49] Fang C, Zheng Y, Chen J, Yam, MCH, Wang W. 2019. Superelastic NiTi SMA cables: thermal-mechanical behavior, hysteretic modelling and seismic application. *Engineering Structures* 183:533-549. doi: 10.1016/j.engstruct.2019.01.049.

[50] Tsai CS, Lee HH. 1993. Applications of viscoelastic dampers to high-rise buildings. *Journal of Structural Engineering* 119(4):1222-1233. doi: 10.1061/(ASCE)0733-9445(1993)119:4(1222)

[51] Zimmer MS. Characterization of viscoelastic materials for use in seismic energy dissipation systems. State University of New York at Buffalo, 1999.

[52] Mazzoni S, McKenna F, Scott M, Fenves G. Open system for earthquake engineering simulation (OpenSees). User command language manual, Pacific Earthquake Engineering Research Center, University of California, Berkeley, 2006.

[53] Xu LH, Fan XW, Li ZX. 2017. Experimental behavior and analysis of self-centering steel brace with pre-pressed disc springs. *Journal of Constructional Steel Research* 139:363–73. doi: 10.1016/j.jcsr.2017.09.021.

[54] Huang X, Eatherton MR, Zhou Z. 2020. Initial stiffness of self-centering systems and application to self-centering-beam moment-frames. *Engineering Structures* 203:109890. doi: 10.1016/j.engstruct.2019.109890.

[55] Mas B, Biggs D, Vieito I, Cladera A, Shaw J, Martínez-Abella F. 2017. Superelastic shape memory alloy cables for reinforced concrete applications. *Construction and Building Materials* 148:307-320. doi: 10.1016/j.conbuildmat.2017.05.041.

[56] Reedlunn B, Daly S, Shaw J. 2013. Superelastic shape memory alloy cables: Part I–isothermal tension experiments. *International Journal of Solids and Structures* 50(20-21):3009-3026. doi: 10.1016/j.ijsolstr.2013.03.013.

[57] Federal Emergency Management Agency (FEMA), FEMA P695, Quantification of Building Seismic Performance Factors, 2009.

[58] Baker JW. 2007. Quantitative classification of near-fault ground motions using wavelet analysis. Bulletin of the Seismological Society of American 97(5):1486-1501. doi: 10.1785/0120060255.

[59] Paul G. Somerville. 2003. Magnitude scaling of the near fault rupture directivity pulse. *Physics of the Earth and Planetary Interiors* 137:201–12. doi: 10.1016/S0031-9201(03)00015-3

[60] Fang C, Ping Y, Chen Y. 2020. Loading protocols for experimental seismic qualification of members in conventional and emerging steel frames. *Earthquake Engineering & Structural Dynamics* 49(2):155-174. doi: 10.1002/eqe.3231

[61] Federal Emergency Management Agency. Seismic Performance Assessment of Buildings, Volume 1 – Methodology, FEMA P-58-1, 2012.

[62] Ruiz-Garcia J, Miranda A. 2006. Residual displacement ratios for assessment of existing structures. *Earthquake Engineering & Structural Dynamics* 35:315-36. doi: 10.1002/eqe.523.

[63] Guo JWW, Christopoulos C. 2018. A probabilistic framework for estimating the residual drift of idealized SDOF systems of non-degrading conventional and damped structures. *Earthquake Engineering & Structural Dynamics* 47(2): 479-496. doi: 10.1002/eqe.2975.

Table 1. Basic information of SMA cables for each SCB

	1.0V frames			0.75V frames		
Floor level	No. of SMA cables	Length of SMA cables (mm)	Total preload (kN)	No. of SMA cables	Length of SMA cable (mm)	Total preload (kN)
1	32	1760	2407	20	1760	1504
2	22	1500	1655	15	1500	1128
3	18	1500	1354	13	1500	978
4	16	1500	1203	12	1500	902
5	16	1500	1203	10	1500	752
6	12	1500	902	9	1500	677
7	10	1500	752	8	1500	602
8	7	1500	526	4	1500	301
9	4	1500	301	2	1500	150

Table 2. Basic information and key analysis results of prototype buildings

				PID (%)		RID (%)		PFA (g)	
Structure type (building code)	Fundamental period (s)	Added damping ratio	Level of base shear	FF	NF	FF	NF	FF	NF
BRBF	1.583	-	1.0V	2.39	3.19	0.49	1.25	0.99	1.00
SCBF	1.583	-	1.0V	3.05	3.65	0.11	0.29	2.22	2.19
HBF-1.0V-0.1	1.558	0.1	1.0V	1.73	2.27	0.05	0.14	1.01	1.07
HBF-1.0V-0.2	1.537	0.2	1.0V	1.57	2.06	0.10	0.34	0.97	0.95
HBF-0.75V-0.1	1.734	0.1	0.75V	1.97	2.44	0.08	0.11	0.90	0.90
HBF-0.75V-0.2	1.701	0.2	0.75V	1.76	2.30	0.10	0.32	0.90	0.88
HBF-0.75V-0.1U	1.748	0.1	0.75V	1.94	2.37	0.06	0.09	0.96	1.00

Table 3. Basic information of viscoelastic materials (length × width, unit in mm)

Floor level	HBF-1.0V-0.1	HBF-1.0V-0.2	HBF-0.75V-0.1	HBF-0.75V-0.2	HBF-0.75V-0.1U
1	500×340	600×570	500×280	600×470	400×165
2	500×240	600×400	500×210	600×350	400×165
3	500×185	600×310	500×180	600×300	400×165
4	500×165	600×275	500×160	600×270	400×165
5	500×160	600×270	500×140	600×235	400×165
6	500×135	600×225	500×125	600×205	400×165
7	250×220	600×190	250×210	600×175	400×165
8	250×150	300×250	250×110	300×180	400×165
9	250×90	300×150	250×70	300×120	400×165

Table 4. Lognormal fitting parameters for R_r values of prototype buildings

	FF		NF	
Building code	μ	σ	μ	σ
BRBF	-1.3701	0.5041	-1.0189	0.4044
SCBF	-3.2429	0.8531	-3.0562	0.9879
HBF-1.0V-0.1	-3.5316	0.7431	-3.0686	0.8063
HBF-1.0V-0.2	-2.9808	0.8873	-2.3262	1.1323
HBF-0.75V-0.1	-3.3884	0.7144	-3.1412	0.7411
HBF-0.75V-0.2	-3.1941	1.0096	-2.4308	1.0506
HBF-0.75V-0.1U	-3.3481	0.4562	-3.3116	0.5862

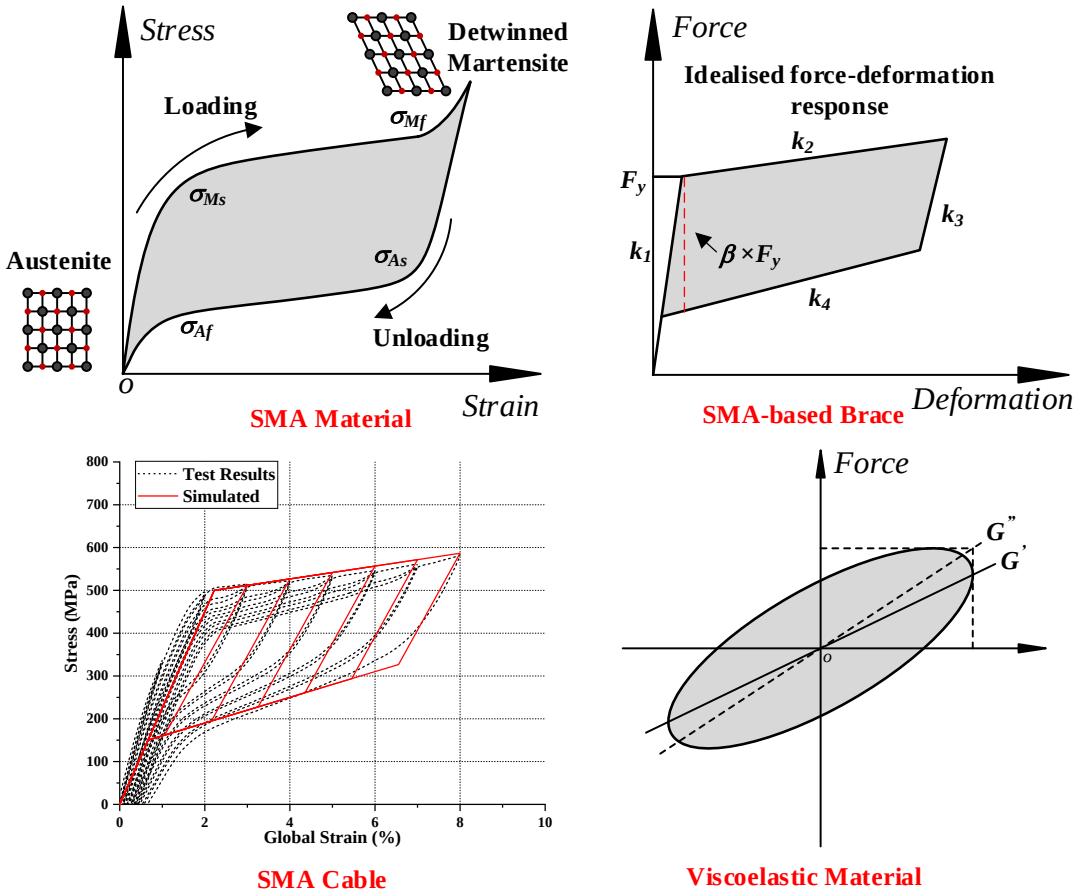

(a)

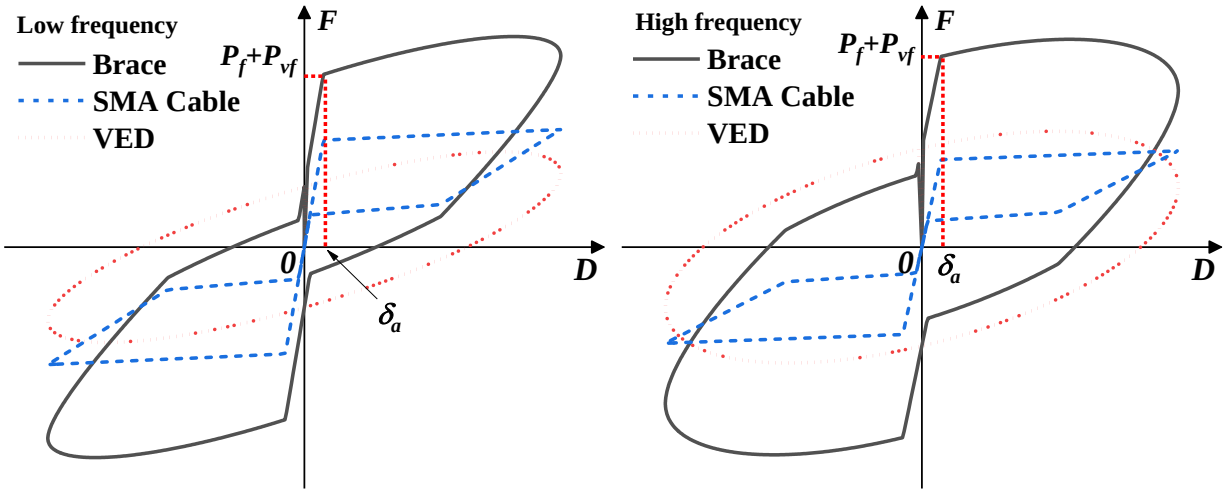

(b)

Figure 1. Fundamental behavior of hybrid brace: a) behavior of superelastic SMA and viscoelastic material, b) influence of loading frequency

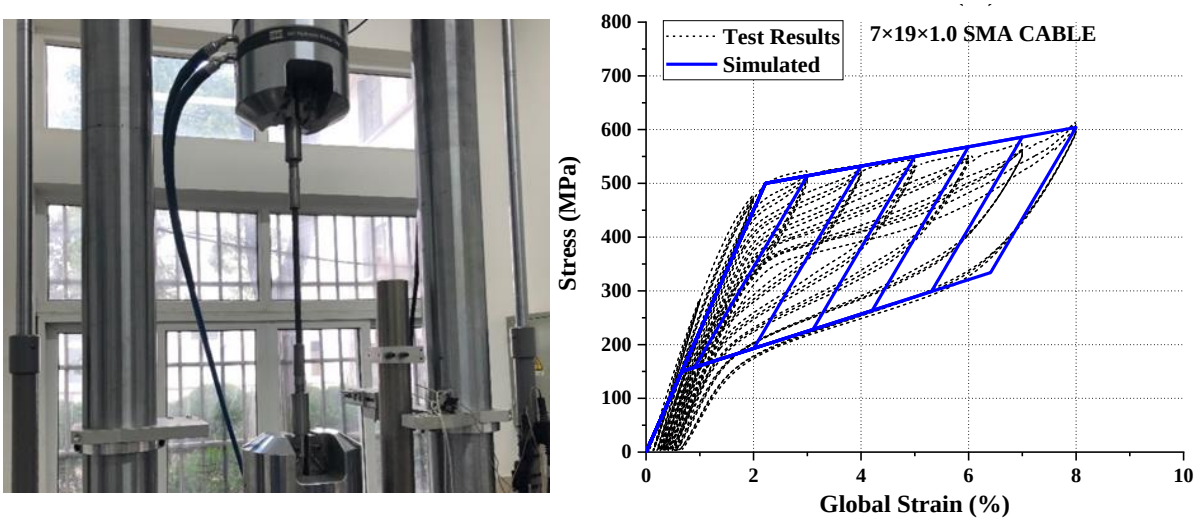

(a)

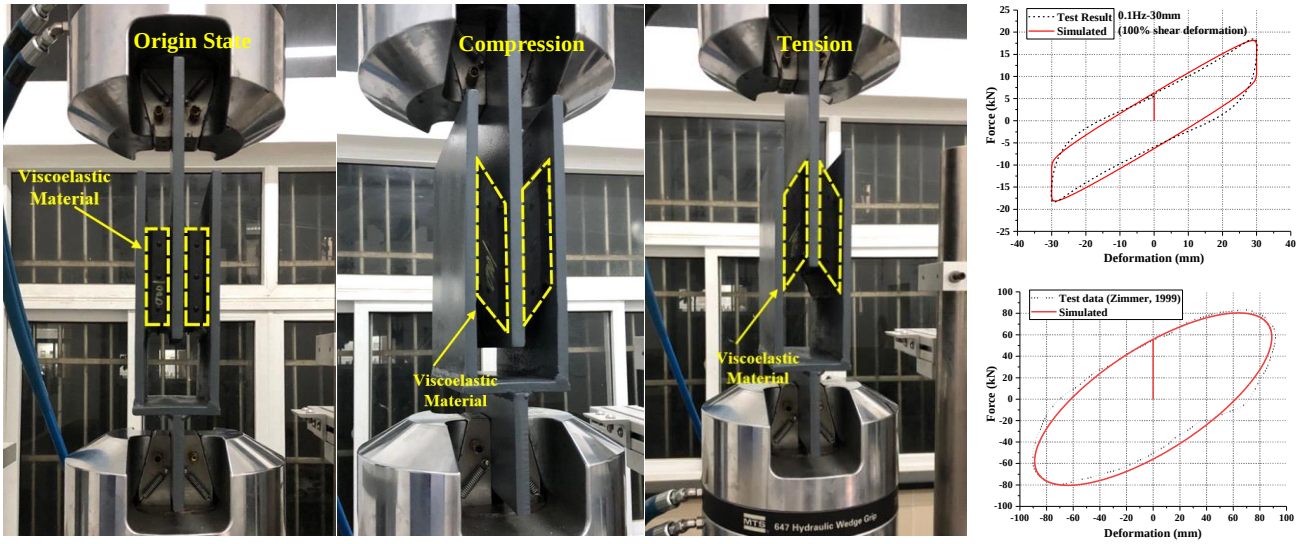

(b)

Figure 2. Typical test results of individual components: a) SMA cable, b) VED

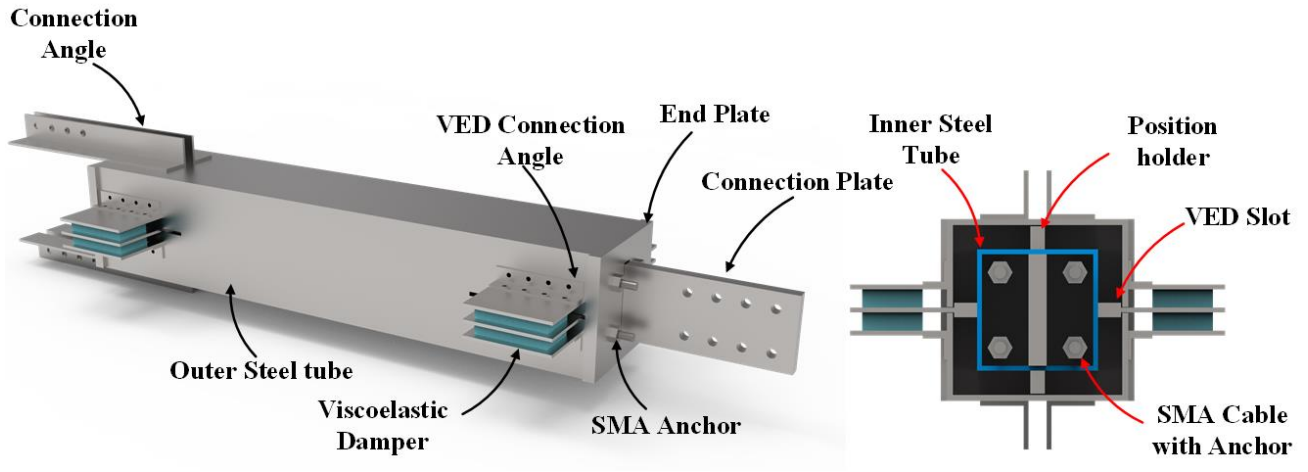

(a)

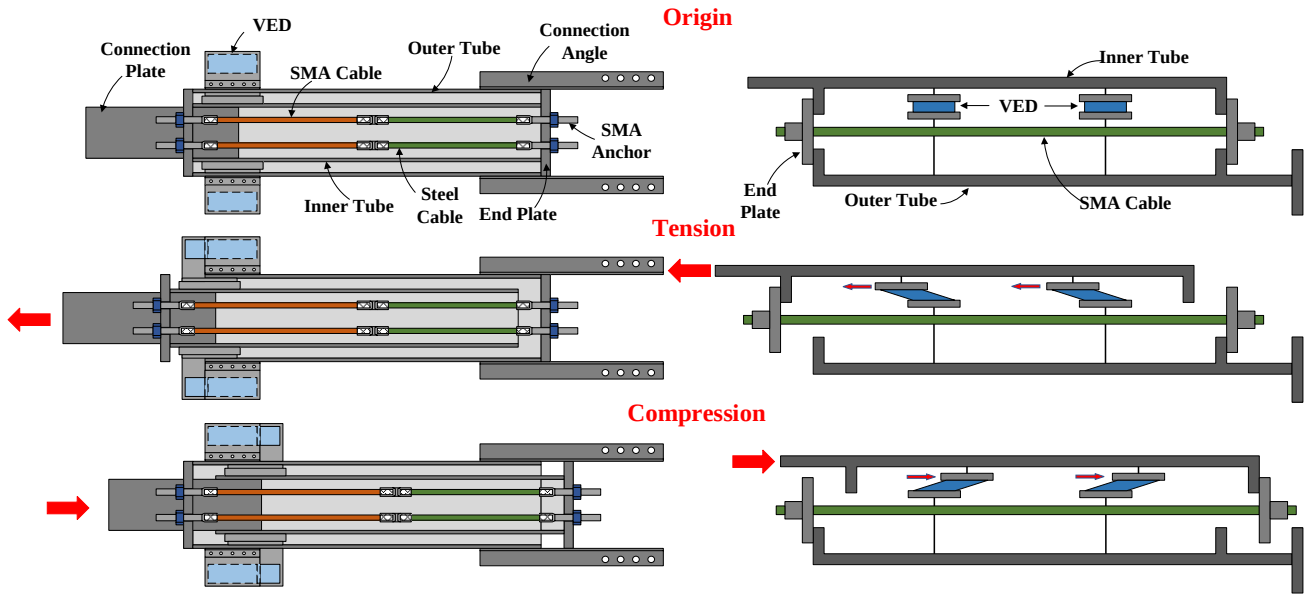

(b)

Figure 3. Hybrid brace with SMA cables: a) basic components and assembly, b) working principle

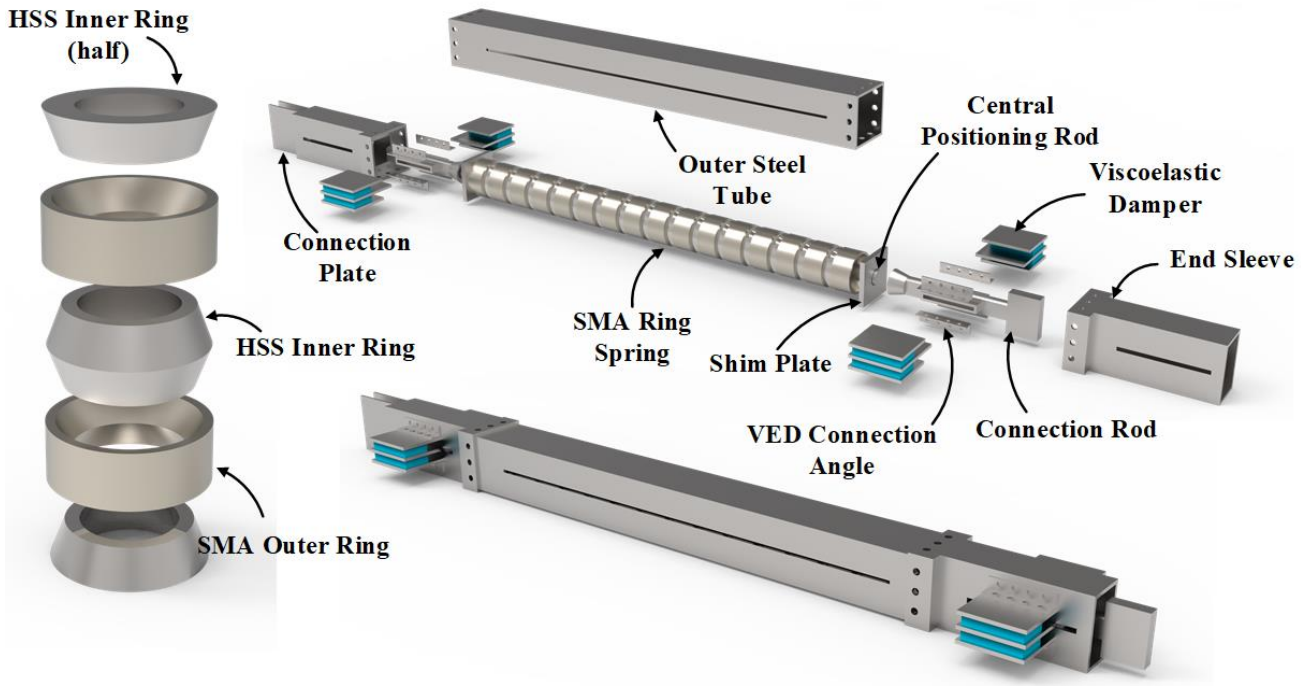

(a)

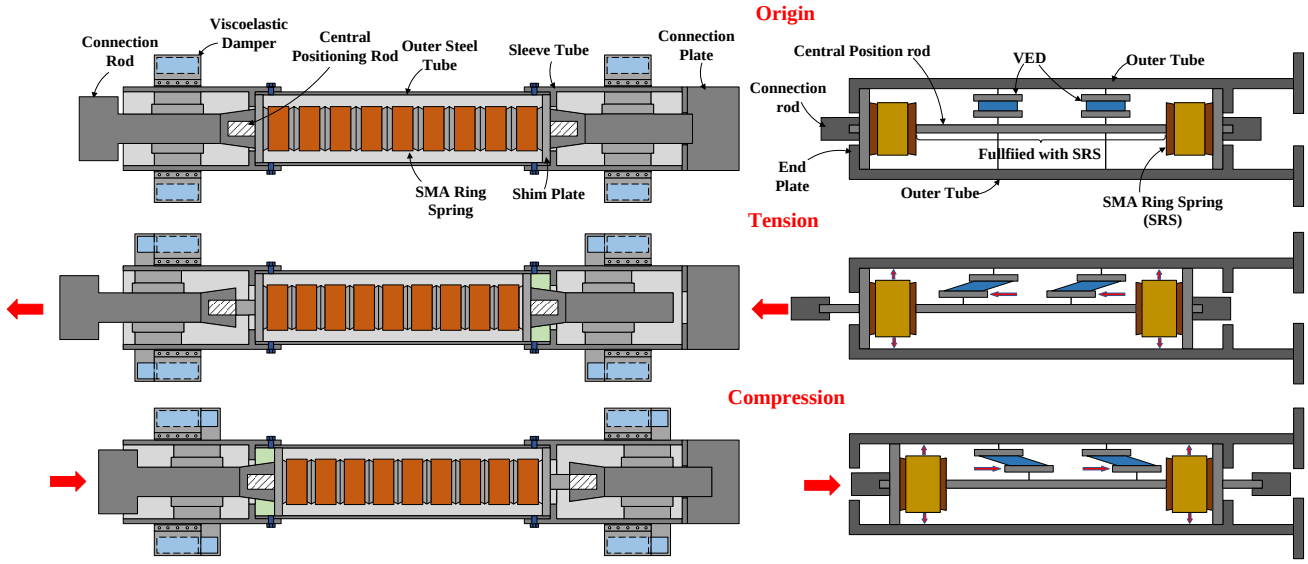

(b)

Figure 4. Hybrid brace with SMA ring springs: a) basic components and assembly, b) working principle

Information of BRB for 2D Frame

Story	Initial Stiffness, kN/mm	Yield Force, kN	Area of steel core, mm^2
1	400.4	2448.2	10418
2	329.6	1706.3	7261
3	256.2	1326.1	5643
4	228.9	1185.1	5043
5	223.6	1157.4	4925
6	185.1	958.1	4077
7	155.4	804.6	3424
8	102.0	528.3	2248
9	61.9	320.3	1363

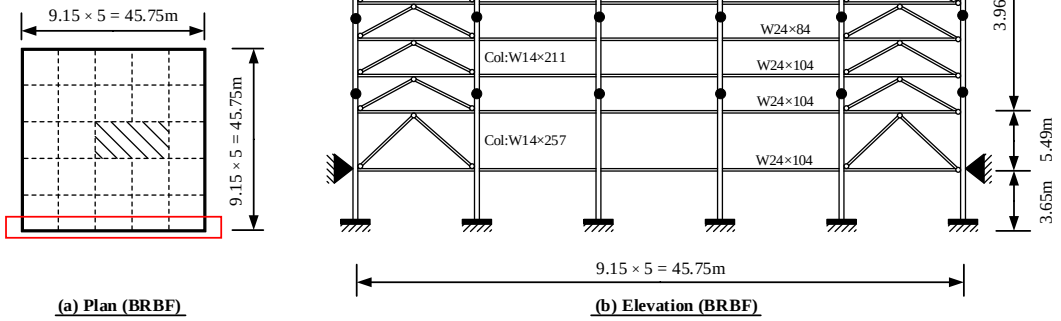

(a) Plan (BRBF) **(b) Elevation (BRBF)**

Figure 5. Basic design information of BRBF

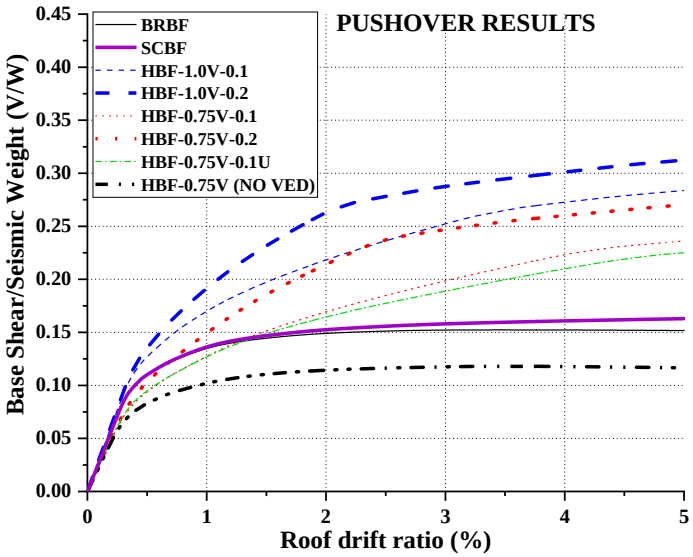

Figure 6. Static pushover curves of prototype buildings

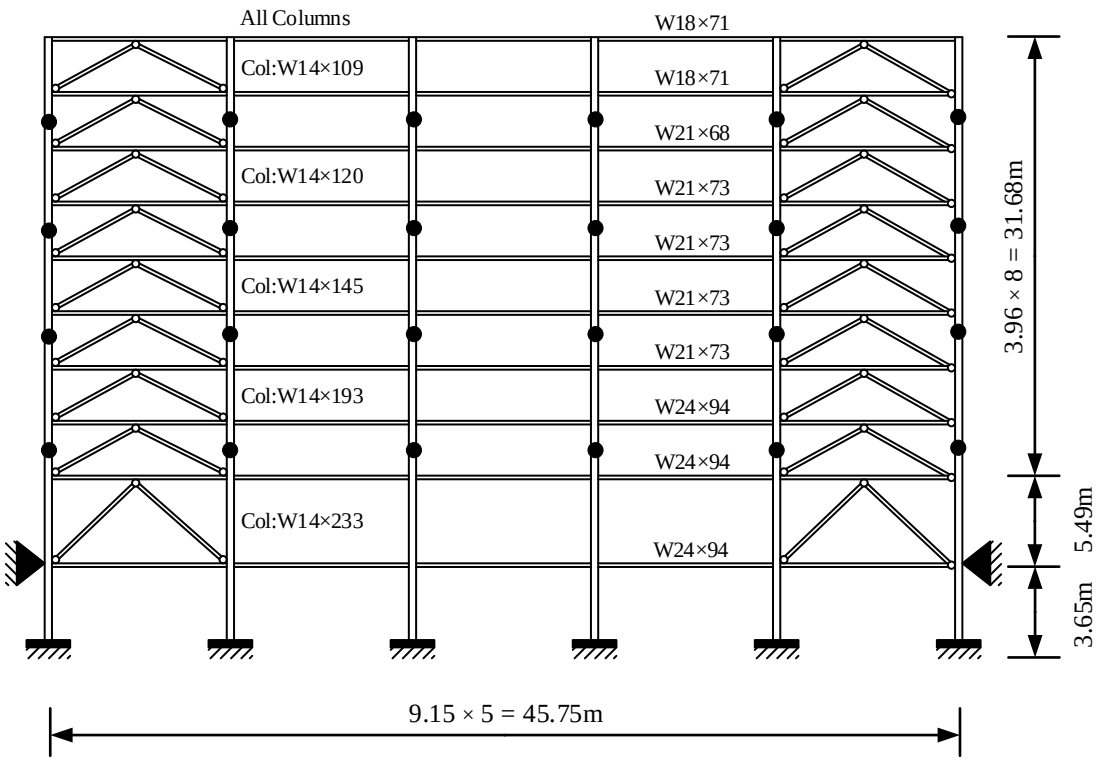

Figure 7. Information of 0.75V frames

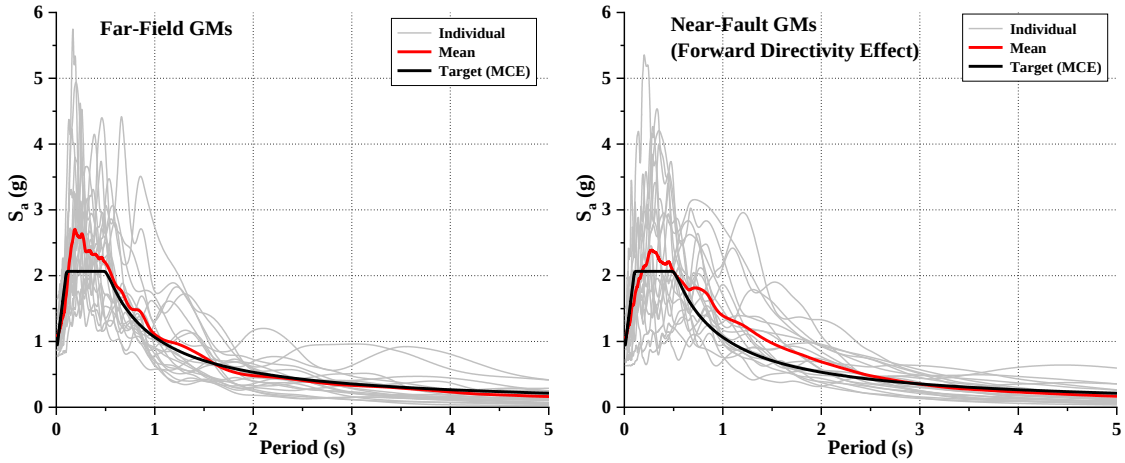

(a) (b)

Figure 8. Response spectra of selected ground motions: a) FF records, b) NF records

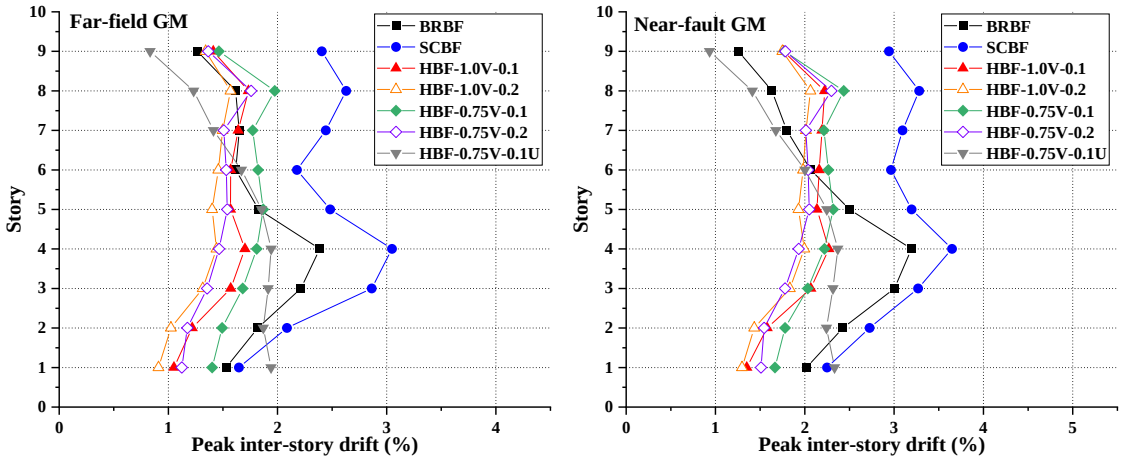

(a)

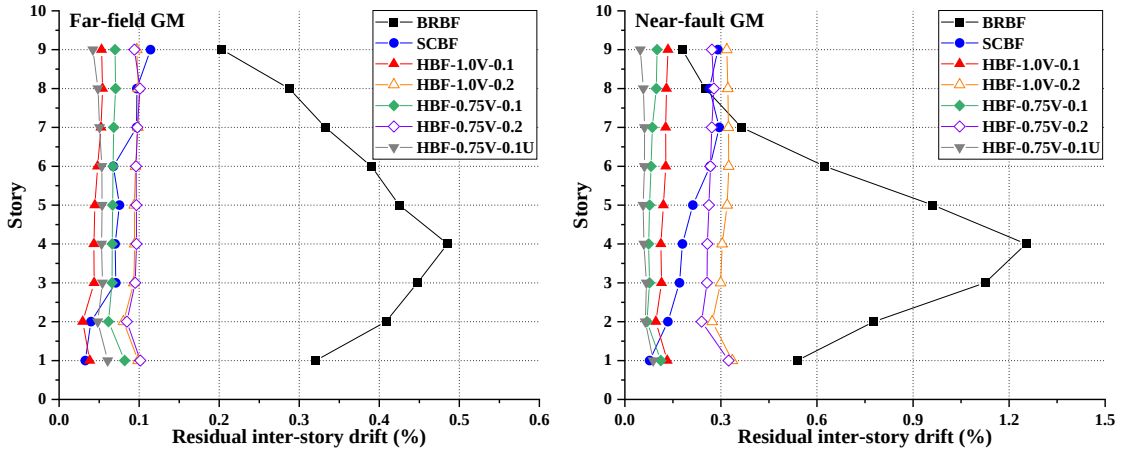

(b)

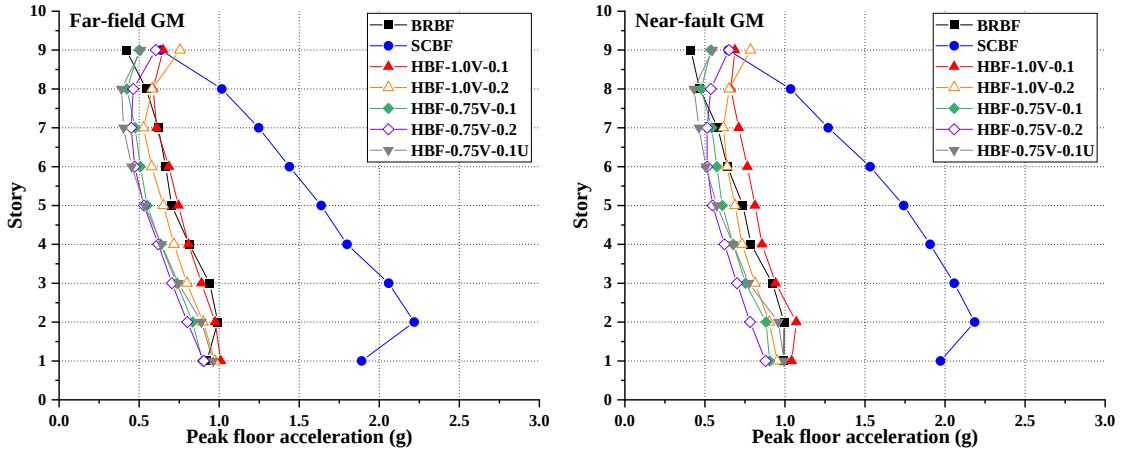

(c)

Figure 9. Mean responses of structures: a) peak inter-story drift (PID), b) residual inter-story drift (RID), c) peak absolute floor acceleration (PFA)

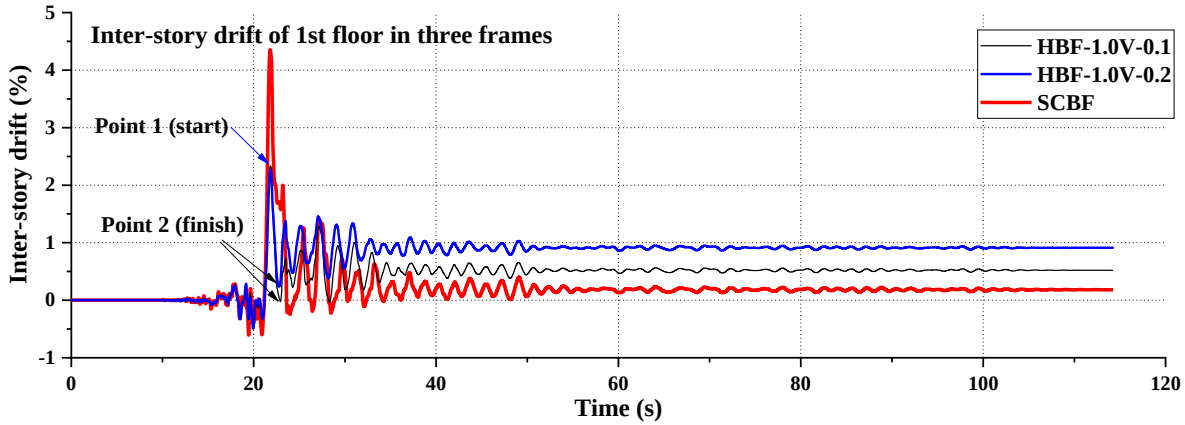

(a)

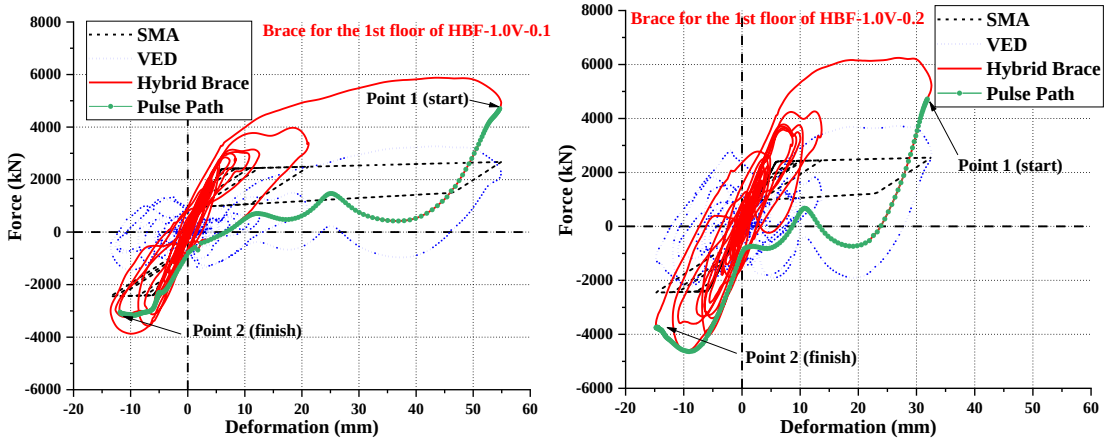

(b)

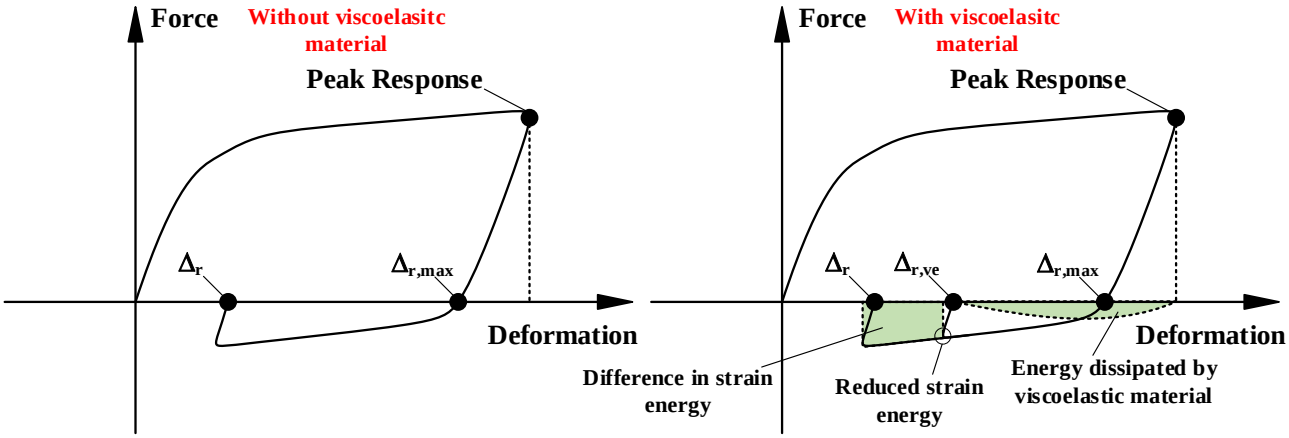

(c)

Figure 10. Influence of added damping ratio on RID: a) inter-story drift time histories, b) force-deformation histories of braces, c) idealized unloading path of boundary frame

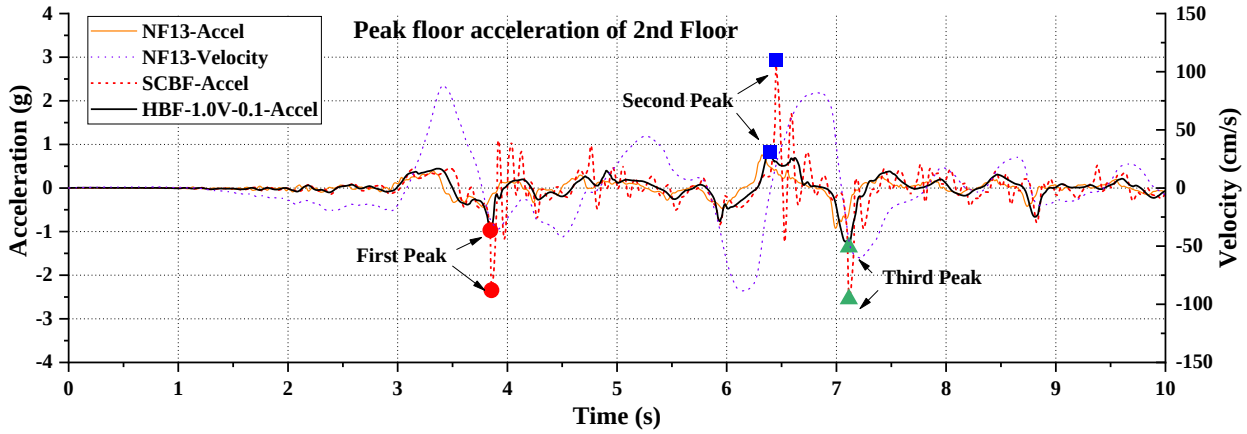

(a)

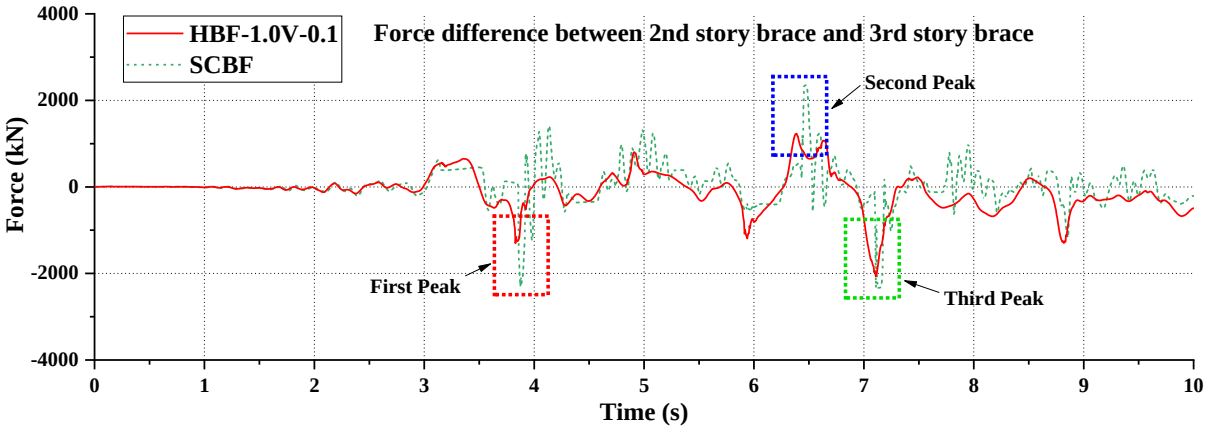

(b)

Figure 11. Influence of added damping ratio on PFA: a) floor acceleration time histories, b) difference of brace force between adjacent floors

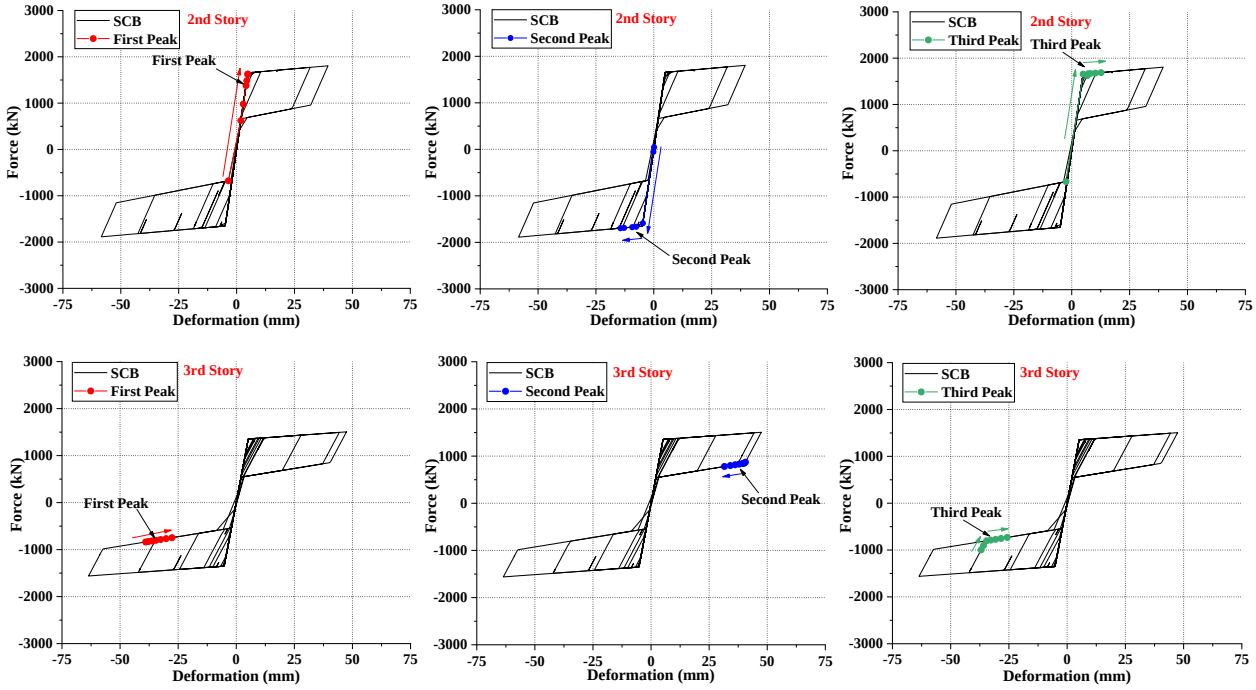

(a)

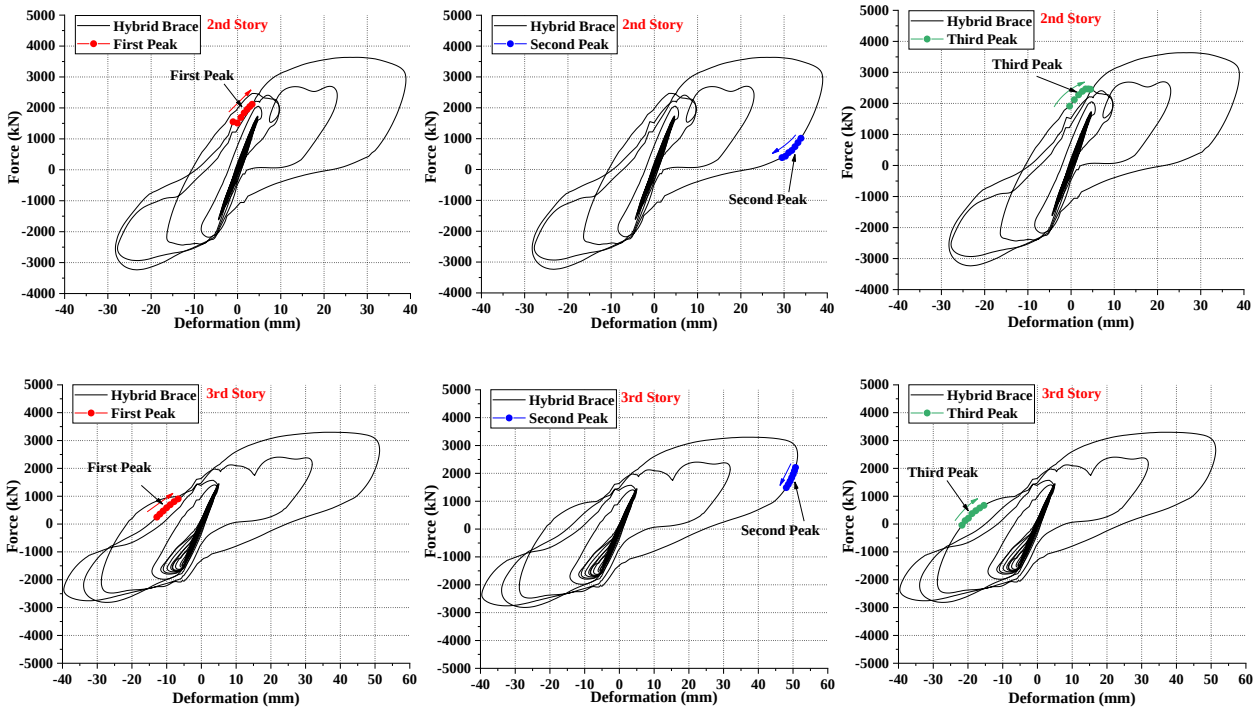

(b)

Figure 12. Force-deformation histories of braces at adjacent floors: a) pure self-centering brace, b) hybrid brace

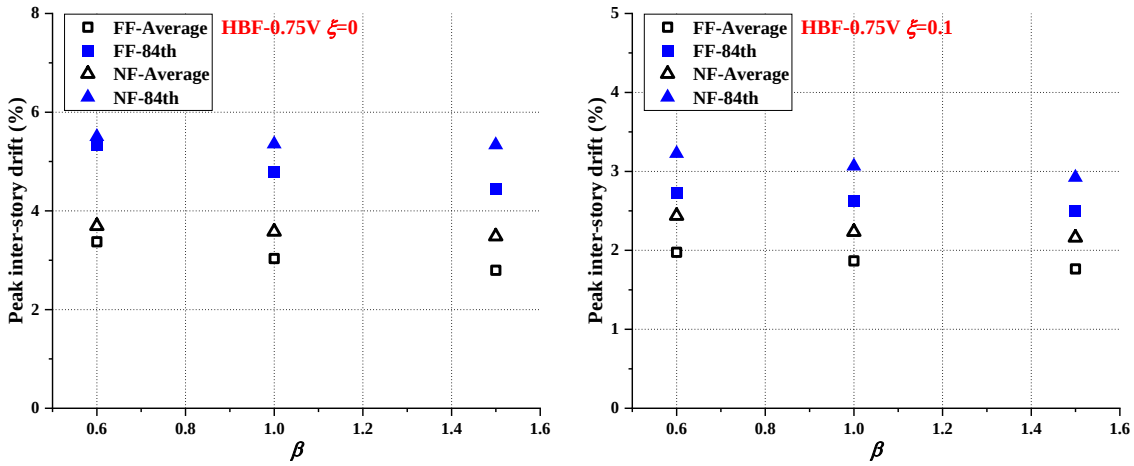

(a)

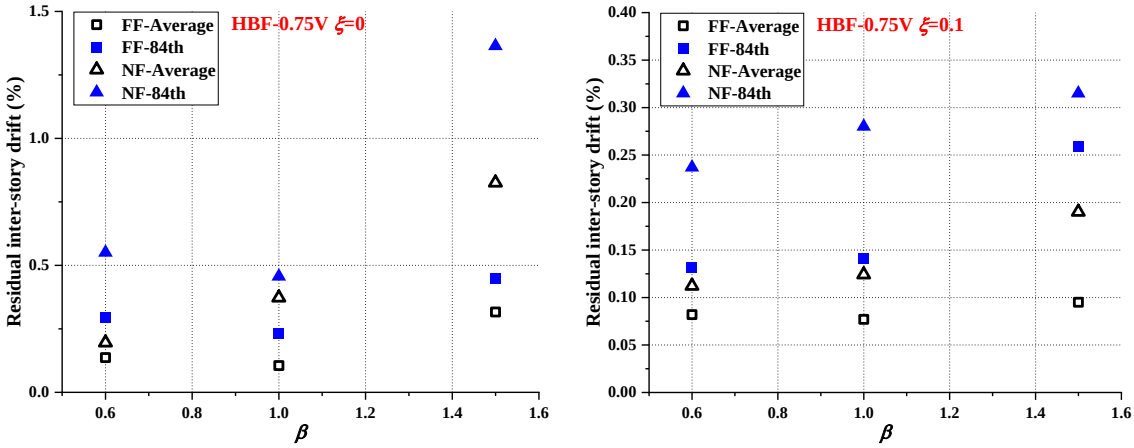

(b)

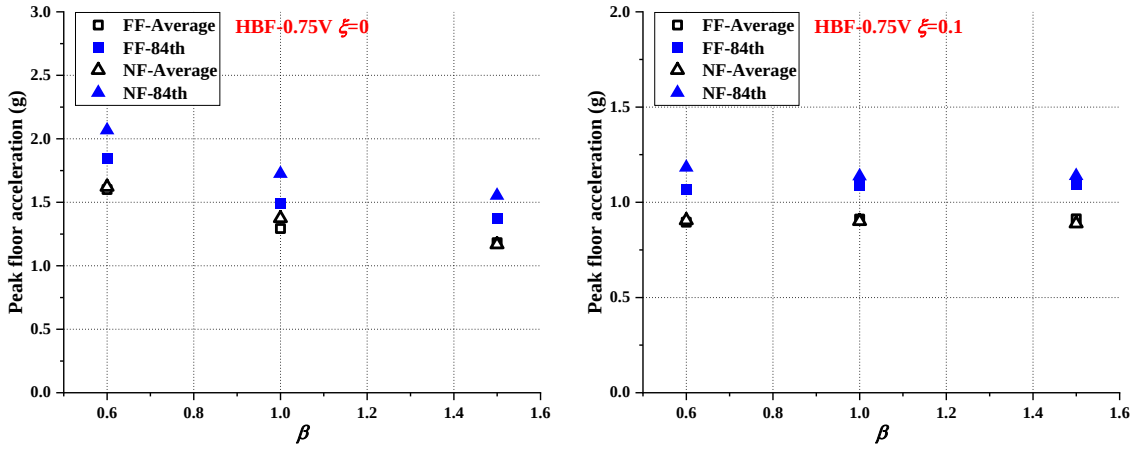

(c)

Figure 13. Influence of β on structural responses: a) PID, b) RID, c) PFA

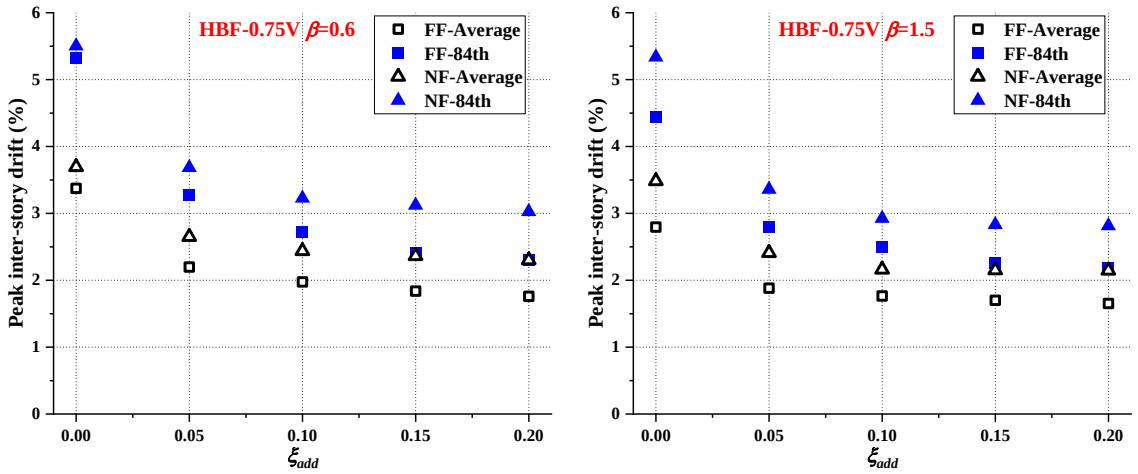

(a)

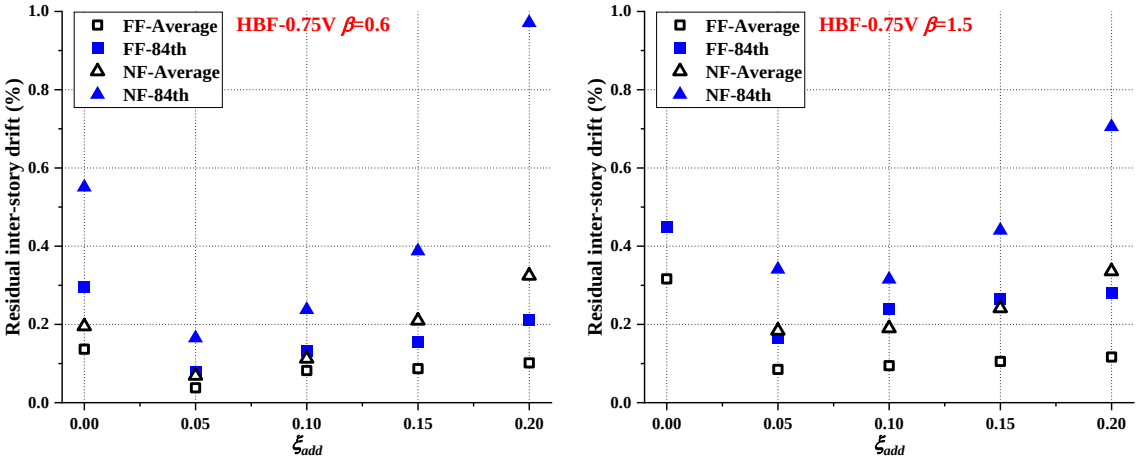

(b)

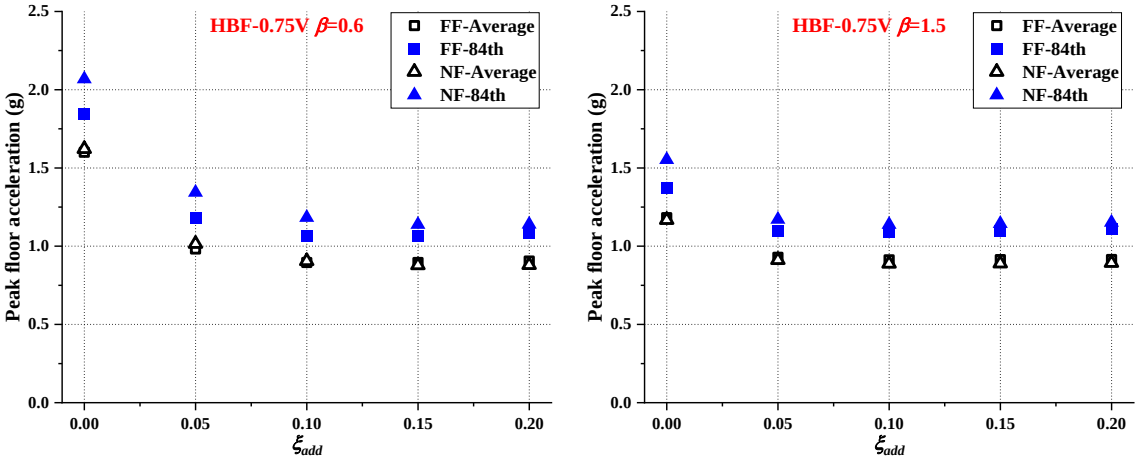

(c)

Figure 14. Influence of ξ_{add} on structural responses: a) PID, b) RID, c) PFA

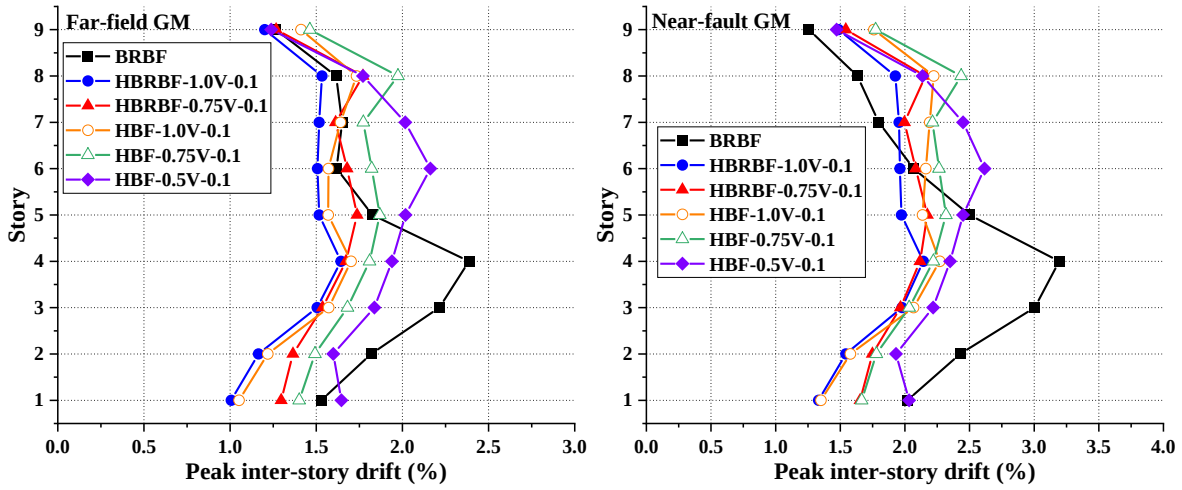

(a)

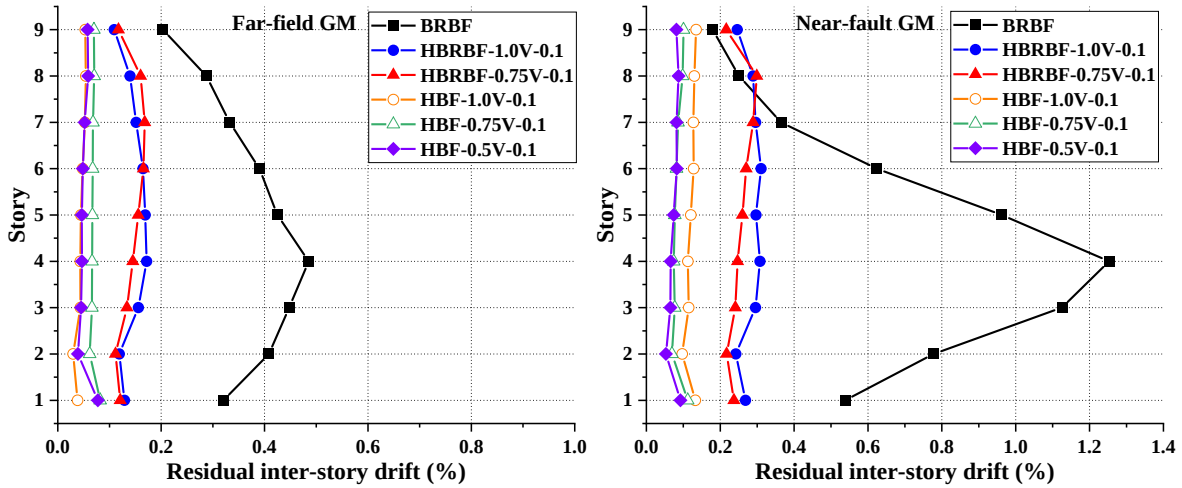

(b)

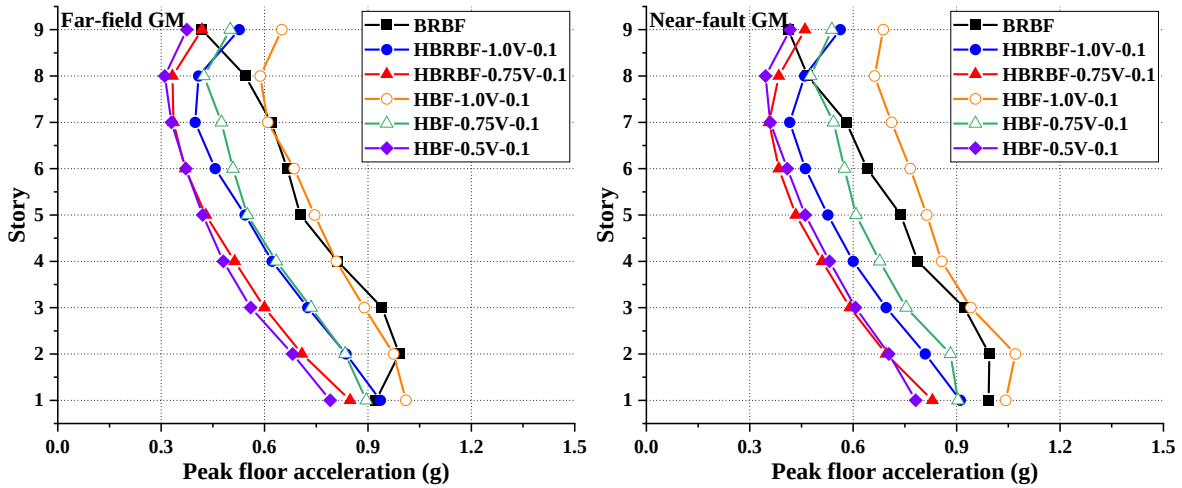

(c)

Figure 15. Mean responses of additionally considered structures: a) peak inter-story drift (PID), b) residual inter-story drift (RID), c) peak absolute floor acceleration (PFA)

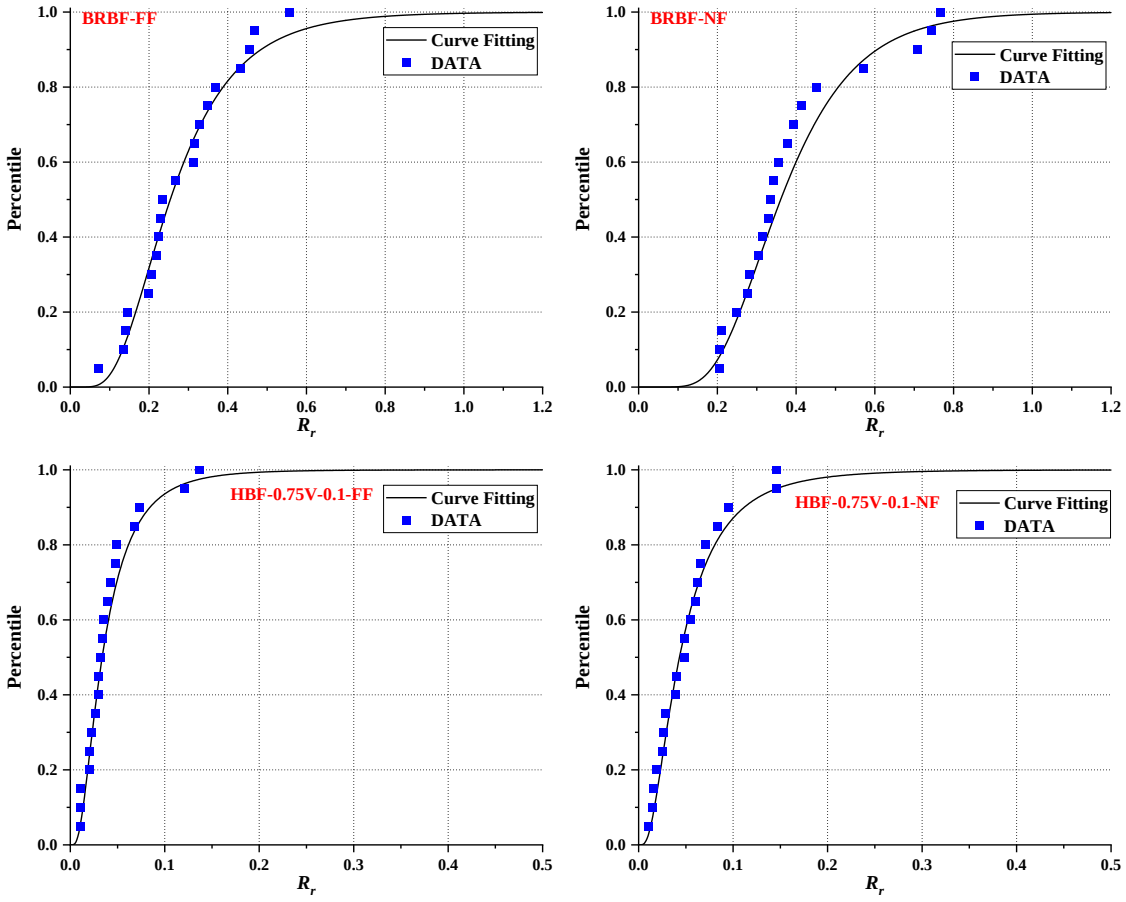

Figure 16. Recorded R_r data and lognormal fitting

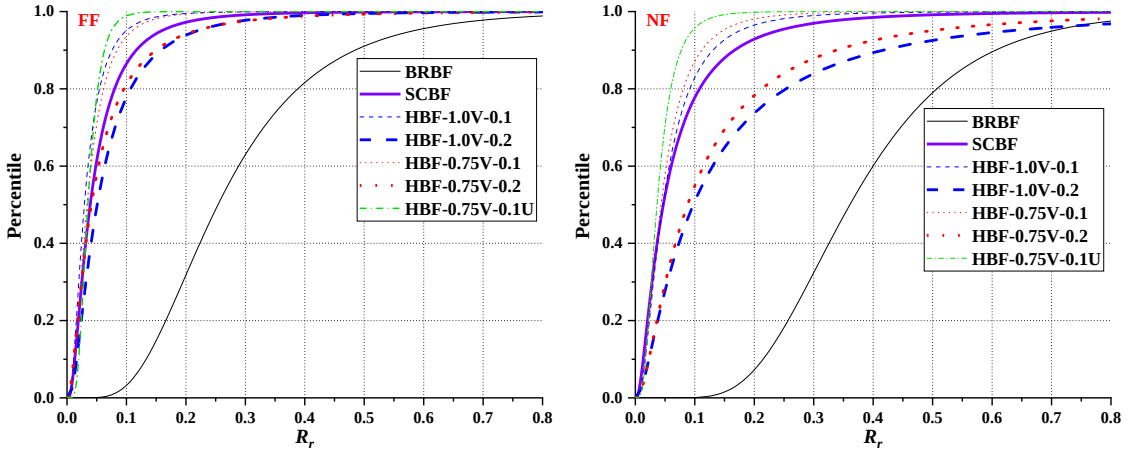

(a)

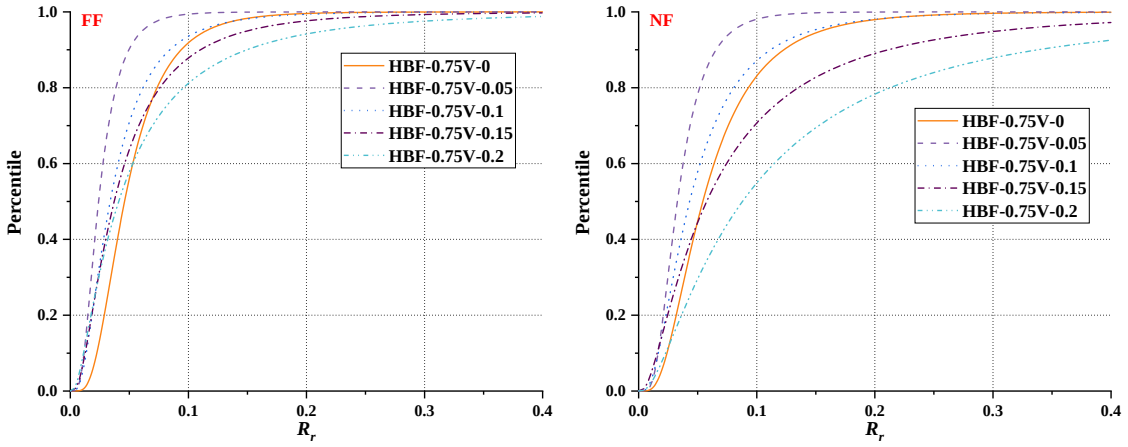

(b)

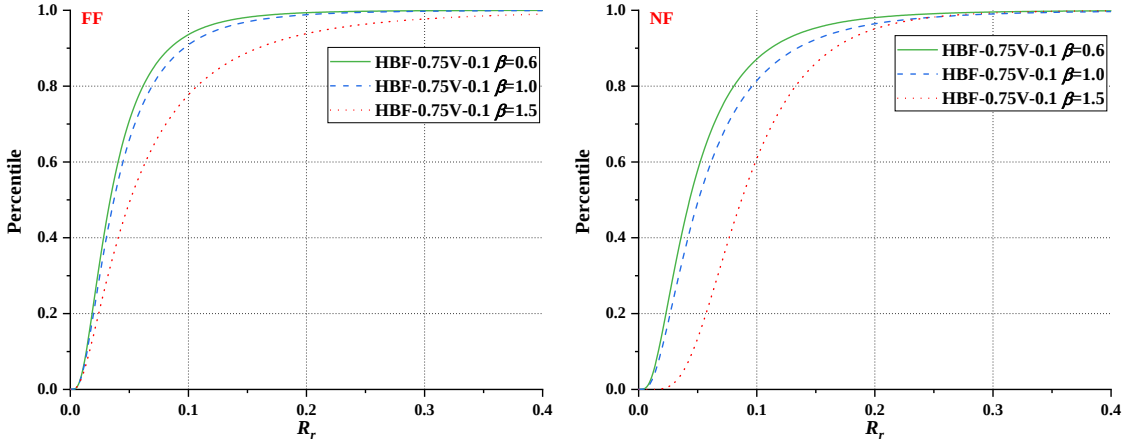

(c)

Figure 17. Cumulative distribution curves of R_r: a) prototype buildings, b) influence of ξ_{add}, c) influence of β

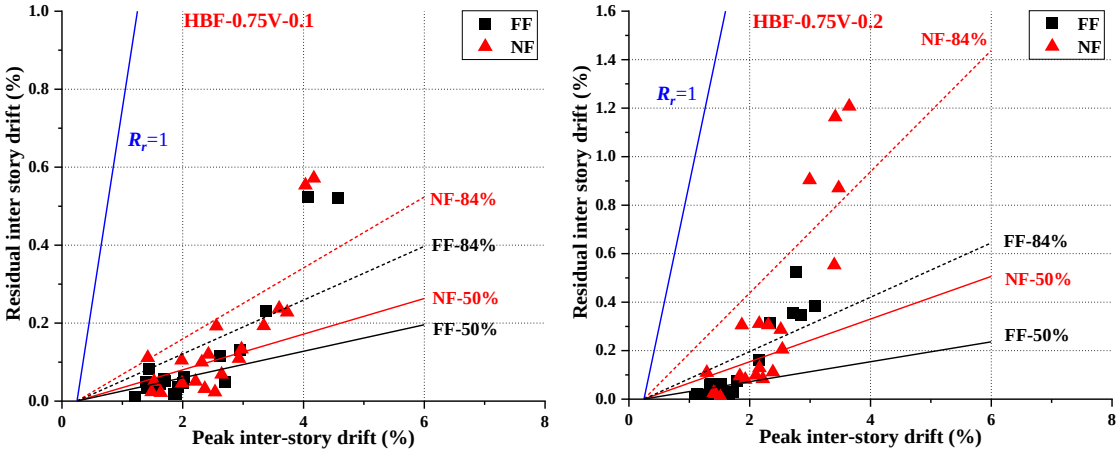

Figure 18. Typical design chart for RID estimation